www.nature.com/nphoton / May 2024 Vol. 18 No. 5

nature photonics

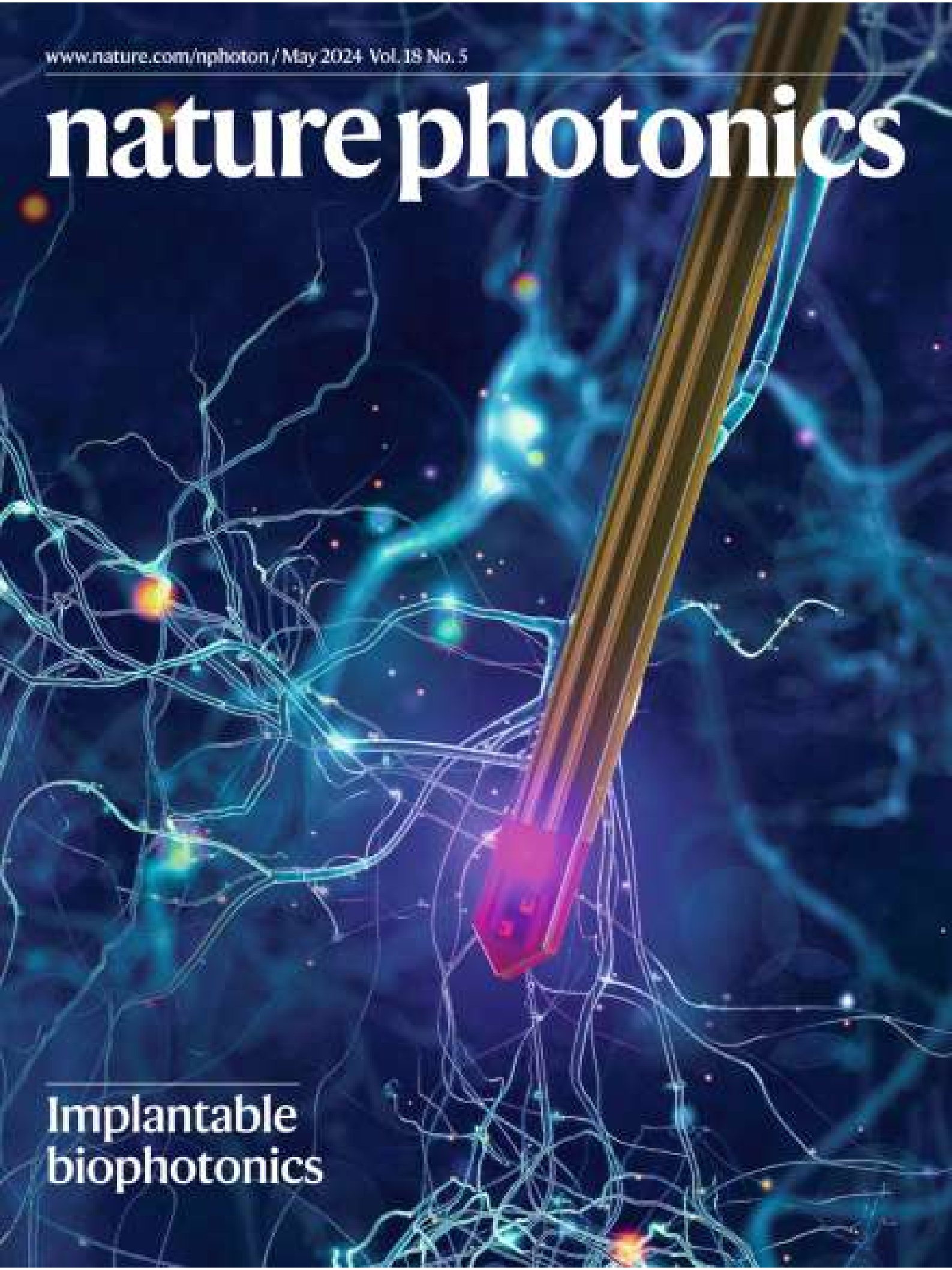

Implantable biophotonics

nature photonics

Article

https://doi.org/10.1038/s41566-023-01374-y

A wireless optoelectronic probe to monitor oxygenation in deep brain tissue

Received: 2 June 2023

Accepted: 18 December 2023

Published online: 24 January 2024

Check for updates

Xue Cai[1,6], Haijian Zhang[2,6], Penghu Wei[3,6], Quanlei Liu[3,6], Dawid Sheng[1], Zhen Li[4], Bozhen Zhang[5], Guo Tang[1], Wenxin Zhao[1], Zhongyin Ye[1], Zhao Xue[2], Yang Xie[1], Yang Dai[3], Changming Wang[3], Yuqi Wang[1], Xin Fu[5], Lan Yin[5], Hongshang Peng[4], He Ding[2] ✉, Guoguang Zhao[3] ✉ & Xing Sheng[1] ✉

Real-time detection of tissue oxygenation in the nervous system is crucial in neuroscience studies and clinical diagnostics. Complementary to blood oxygenation levels, the partial pressure of oxygen in brain tissue (p_{btO_2}) plays a key role in regulating local neural activities and metabolism. Here we develop an implantable optoelectronic probe that wirelessly and continuously monitors p_{btO_2} signals in the deep brain of freely moving rodents. The thin-film, microscale implant integrates a light-emitting diode and a photodetector, and is coated with an oxygen-sensitive phosphorescent film. Powered by a battery or an inductive coil, a miniaturized circuit is capable of recording and wirelessly transmitting p_{btO_2} signals. The wireless micro-probe captures cerebral hypoxia states in mice in various scenarios, including altered inspired oxygen concentrations and acute ischaemia. In mouse models with seizures, the micro-probe associates temporal p_{btO_2} variations in multiple brain regions with electrical stimulations applied to the hippocampus. Our probe and method offer important insights into neuroscience studies regarding neurometabolic coupling and pave the way for the clinical application of implantable wireless optoelectronic probes.

The supply of oxygen (O_2) is vital in human metabolism. Hypoxia, in which tissue oxygenation is below the normal level, can cause the dysfunction of, damage to and even the death of biological cells and organs[1,2]. As a leading consumer of O_2, the human brain, which constitutes only ~2% of the body weight, expends ~20% of the body's total O_2 supply to continuously maintain its normal function[3]. Cerebral hypoxia, which is caused by acute brain abnormalities such as poisoning, traumatic brain injury and subarachnoid haemorrhage[4–6] or diseases including hydrocephalus and brain tumours[7,8], can lead to irreversible damage of the brain function and result in disability and death. In addition, cerebral hypoxia is closely associated with neurological and cerebrovascular diseases such as epilepsy and apoplexy, as well as various neurodegenerative disorders[9,10]. Therefore, real-time monitoring of the cerebral oxygenation state is crucial, not only for understanding the metabolic coupling between O_2 and brain activities but also for improving clinical practices[11,12].

[1]Department of Electronic Engineering, Beijing National Research Center for Information Science and Technology, Institute for Precision Medicine, Laboratory of Flexible Electronics Technology, IDG/McGovern Institute for Brain Research, Tsinghua University, Beijing, China. [2]Beijing Engineering Research Center of Mixed Reality and Advanced Display, School of Optics and Photonics, Beijing Institute of Technology, Beijing, China. [3]Department of Neurosurgery, Xuanwu Hospital of Capital Medical University, National Medical Center for Neurological Diseases, Beijing, China. [4]Engineering Research Center of Photonic Design Software, Ministry of Education, Minzu University of China, Beijing, China. [5]School of Materials Science and Engineering, The Key Laboratory of Advanced Materials of Ministry of Education, State Key Laboratory of New Ceramics and Fine Processing, Laboratory of Flexible Electronics Technology, Tsinghua University, Beijing, China. [6]These authors contributed equally: Xue Cai, Haijian Zhang, Penghu Wei, Quanlei Liu. ✉e-mail: heding@bit.edu.cn; ggzhao@vip.sina.com; xingsheng@tsinghua.edu.cn

Conventional biological techniques that detect O_2 in the brain mostly rely on near-infrared spectroscopy and functional magnetic resonance imaging[13,14]. Near-infrared spectroscopy, along with other recently reported invasive O_2-sensing probes[15,16], assesses the cerebral blood oxygen saturation (S_{tO_2}) by exploiting the difference in optical absorption between oxygenated and deoxygenated haemoglobin (HbO_2 and Hb, respectively)[17]. Alternatively, blood-oxygen-level-dependent (or BOLD) imaging in functional magnetic resonance imaging focuses primarily on the concentration of Hb in the blood flow[18]. Whereas S_{tO_2} reflects the concentrations of Hb and HbO_2 in the blood transported through the vessels, its value sometimes deviates from the partial pressure of O_2 in brain tissue (p_{btO_2})[19]. Non-invasive methods for direct p_{btO_2} detection involve electron paramagnetic resonance[20] and positron emission tomography[21], which rely on injected or inhaled O_2 tracers that delay the detection of p_{btO_2} and bulky, high-cost instruments that prohibit portable use.

To measure local p_{btO_2} signals, clinically available techniques utilize the insertion of electrochemical or optical probes into the targeted region. Electrochemical methods based on polarographic analyses use Clark-type electrodes or other conductive wires to detect p_{btO_2} signals via oxidative reactions[22–25]. These chemical electrodes typically consume O_2 during detection, require a certain time to stabilize and are vulnerable to contamination from interfering substances in the absence of a carefully designed O_2-selective membrane[25,26]. Optical techniques leverage phosphorescent dyes whose luminescence efficiencies or lifetimes decay with the addition of O_2 (ref. 27), so that the tissue oxygenation can be sensed via imaging or spectroscopic setups[28,29]. Compared with electrochemical probes, the luminescence quenching process exhibits superior O_2 selectivity and promising resistance to electromagnetic interference[3,29,30]. Traditional tools based on this mechanism for the sensing of O_2 utilize tethered fibre-optic systems for light delivery and collection[30,31]. A recent study has demonstrated optical-based O_2 sensing in the deep peripheral tissue in living sheep using an ultrasound-powered optoelectronic device[32]; however, its deployment in the deep brain has not yet been accomplished.

Here we present a microscale, optoelectronic probe that wirelessly monitors in vivo p_{btO_2} signals in real time. The micro-probe measures local p_{btO_2} levels based on the quenching of phosphorescent dyes, whose optical signals are excited and collected via integrating a light-emitting diode (LED) and a photodetector. Miniaturized circuits, which can be powered using a battery or an inductive coil, capture and wirelessly transmit the p_{btO_2} data. In vitro and in vivo studies reveal the system's capability of dynamic p_{btO_2} recording, and the probe captures the cerebral hypoxia conditions with electrophysiological activities in a rodent seizure model.

Results

The microscale optoelectronic probe for p_{btO_2} monitoring

We designed and fabricated a microscale optoelectronic probe to monitor p_{btO_2} changes in the deep brain (Fig. 1a,b). The detailed probe design and fabrication procedures are described in the Methods and Extended Data Fig. 1. From top to bottom (Fig. 1b), the micro-probe consists of a polydimethylsiloxane (PDMS) film embedded with platinum(II)-5,10,15,20-tetrakis-(2,3,4,5,6-pentafluorphenyl)-porphyrin (PtTFPP) phosphorescent dye, a PDMS/parylene encapsulation layer, an indium gallium nitride (InGaN) violet LED, a dielectric filter and an indium gallium phosphide (InGaP) photodetector on a copper-coated polyimide (PI) substrate. The sensing mechanism for P_{btO_2} operates on the principle of the photoluminescence (PL) quenching of PtTFPP with an increased level of p_{O_2} (ref. 33) (Fig. 1c,d). PtTFPP, at a concentration of 0.1 wt%, is mixed into the PDMS coating layer to obtain the optimal absorption and emission properties (Extended Data Fig. 2). The PtTFPP/PDMS film absorbs violet light (with an absorption peak at 389 nm) and shows a red PL emission peak at 646 nm (Fig. 1e). With an electroluminescence peak wavelength of 395 nm, the InGaN violet LED serves as an excitation source for PtTFPP, whose PL emission is captured by the InGaP detector. Compared with previously reported implantable detectors based on silicon[16] or gallium arsenide (GaAs)[34], the InGaP photodiode has a larger bandgap and therefore a smaller dark current density. In addition, InGaP is more stable than silicon and is less toxic than GaAs. The multilayered silicon dioxide/titanium dioxide-based longpass filter on the InGaP detector effectively optimizes its sensitivity in the red spectral range, resulting in a band-selective absorption between 570 and 655 nm. More details of these optical components are provided in the Methods, Extended Data Figs. 3 and 4 and Supplementary Tables 1 and 2. Collectively, the LED and the detector exhibit optical characteristics that are well-suited to the properties of PtTFPP (Fig. 1f). Figure 1g displays images of a fully integrated p_{btO_2} -sensing probe, and the PtTFPP/PDMS coating is approximately 30 µm thick (Supplementary Fig. 1). On changing the environment from air to pure nitrogen (N_2), the micro-probe exhibits a stronger red phosphorescence emission. Similar responses are observed when the micro-probe is inserted into a brain phantom, as shown in Fig. 1h.

Furthermore, we established optical models to simulate the light distributions within the micro-probe and the surrounding tissue (Fig. 1i). Figure 1j demonstrates that the violet emission from the LED is predominantly absorbed by the PtTFPP/PDMS coating, with almost no leakage of PtTFPP into the surrounding tissue. By contrast, the down-converted red phosphorescence emitted by PtTFPP can penetrate more deeply into the tissue and be partially captured by the adjacent detector (Fig. 1k).

In vitro performance of the p_{btO_2}-sensing probe

We evaluated the performance of the micro-probe in a gas chamber with various O_2 partial pressures (p_{O_2}) by mixing N_2 and O_2 gas flows (Fig. 2a). At an LED injection current of 0.5 mA, the detector collects the PL intensity of the PtTFPP/PDMS coating at p_{O_2} levels from 0 to 70 mm Hg (Fig. 2b and Supplementary Fig. 2). The non-zero signals captured at high O_2 pressure are mainly induced by the leaked violet light (Supplementary Fig. 3). The inverse of the PL intensity is linearly dependent on p_{O_2} and follows the Stern–Volmer equation (Fig. 2c)[17]. The nonlinear relationship between the PL intensity and p_{O_2} shows that the micro-probe is more sensitive to O_2 fluctuations at lower p_{O_2} levels. At room temperature, the measured p_{O_2} detection resolutions are <0.8 mm Hg at p_{O_2} = 3.8 mm Hg and <13 mm Hg at p_{O_2} = 56 mm Hg (Supplementary Fig. 2). We also examined the dynamic response of the micro-probe to multiple cycles of alternated O_2 and N_2 flows (Fig. 2d). When the gas flow (10 litres per min) is switched between O_2 and N_2, the recorded signal rise and decay times are 15.7 s and 0.9 s, respectively (Fig. 2e). The transient response of our micro-probe system is faster than previously reported techniques based on optical sensors and Clark electrodes[23,31,32,35,36]. In addition, the PL quenching mechanism in PtTFPP ensures that the micro-probe possesses high O_2 selectivity over other gases, including N_2 and CO_2 (Fig. 2f). After the pretreatment, the micro-probe can continuously monitor p_{O_2} for over 2 h without any substantial photobleaching (Fig. 2g). Besides photostability, the micro-probe also exhibits desirable thermal stability (Fig. 2h). During in vitro and in vivo operation, the LED is driven by a pulsed current of 0.5 mA, which leads to a temperature rise of less than 1 °C (Supplementary Fig. 4). Therefore, the heating of the device has a minimal effect on the measurement accuracy and normal tissue function. Finally, the absorption of the PtTFPP/PDMS coating remains unchanged when immersed in phosphate-buffered saline (PBS) solution for over a month (Fig. 2i and Supplementary Fig. 5).

Real-time, in vivo p_{btO_2} monitoring with the wireless probe

For continuous p_{btO_2} monitoring in living animals, we applied the implantable optoelectronic probe with a customized wireless control circuit. As shown in Fig. 3a, the key components in the circuit involve

https://doi.org/10.1038/s41566-023-01374-y

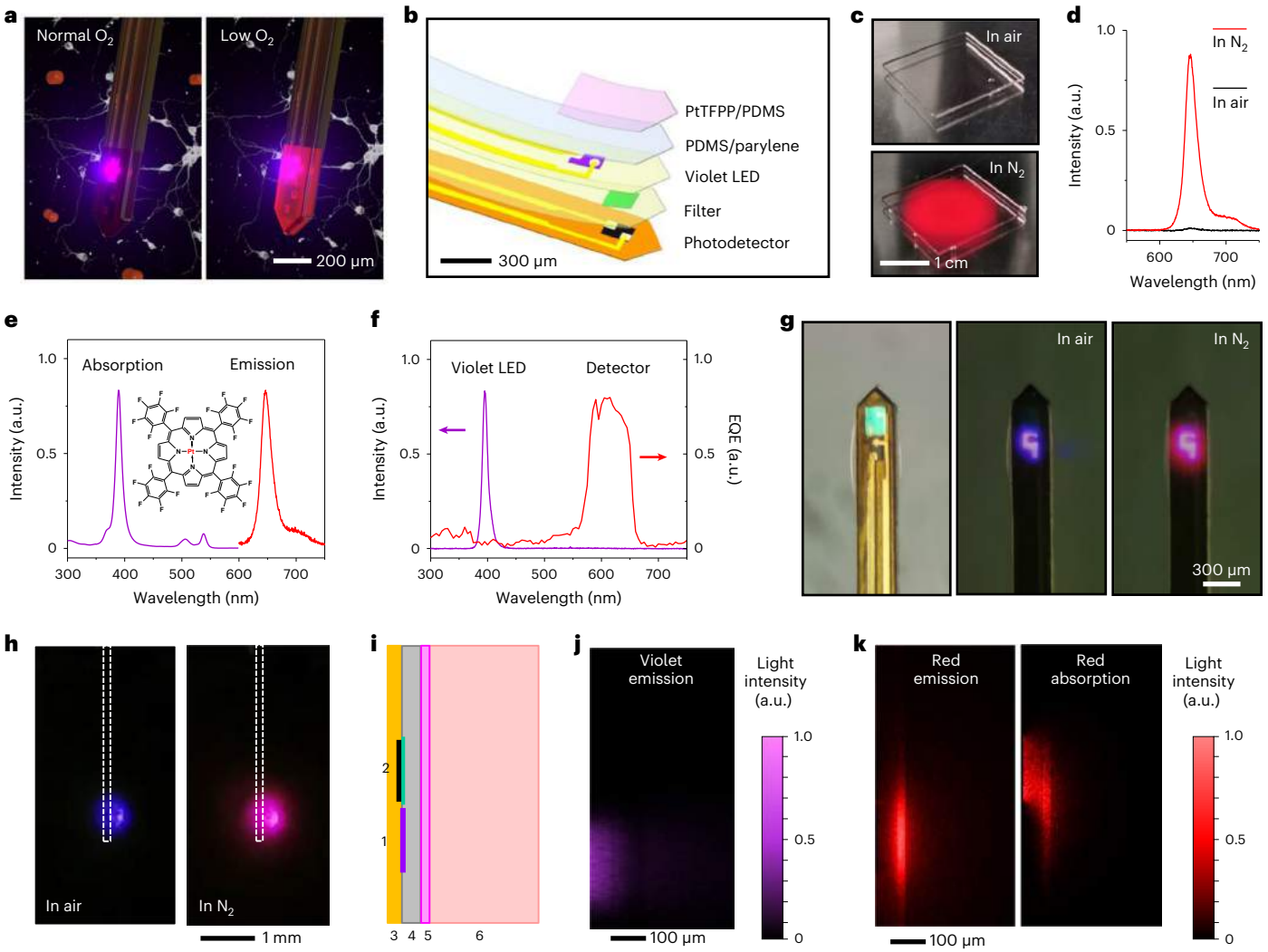

Fig. 1 | Microscale optoelectronic probe for monitoring the oxygenation of brain tissue (p_{btO_2}). **a**, Schematic illustration of the probe implanted into brain tissue and optically responding to the change in O_2 concentration (left: normal conditions; right: low O_2 concentration). **b**, Enlarged view of the probe design, which includes (from top to bottom) a PtTFPP/PDMS sensing film, a PDMS/parylene encapsulation layer, an InGaN violet LED, a filter and an InGaP photodetector on a PI substrate. **c**, Photographs of a PtTFPP/PDMS film excited by violet light in air (top) and in a pure N_2 environment (bottom). **d**, PL spectra of the PtTFPP/PDMS film in air and in N_2. **e**, Absorption and PL spectra of PtTFPP in PDMS. Inset: molecular structure of PtTFPP. **f**, Electroluminescence spectrum of the violet LED and the external quantum efficiency (EQE) spectrum of the detector with a filter. **g**, Top-view optical images of a probe (left: LED is off; middle: LED is on in air; right: LED is on in N_2). **h**, Experimental photographs comparing the light emission from a probe (side-view) implanted in a brain phantom in air (left) and in pure N_2 (right). **i**, Schematic of the probe structure (side-view) used in the optical modelling: (1) LED; (2) detector with filter; (3) PI; (4) PDMS/parylene; (5) PtTFPP/PDMS; (6) brain tissue. **j**, Simulated intensity distribution of the violet excitation light from the LED. **k**, Simulated red PL emission from the PtTFPP dye (left) and that captured by the detector (right) in N_2.

an LED driver, an operational amplifier, a Bluetooth system on chip and a rechargeable battery. Data are converted to the corresponding p_{btO_2} values on the basis of in vitro calibrations for individual probes. The circuit module has a compact size of 12.3 × 17.3 mm^2 and a weight of 1.8 g (Fig. 3b, Supplementary Figs. 6 and 7 and Supplementary Table 3), and it is head-mounted on a freely moving mouse for the continuous monitoring of p_{btO_2} (Fig. 3c). To assess the sensing capability, we conducted acute tests on a mouse by dynamically varying the fraction of inspired O_2 (F_{iO_2}) using a mixture of inhaled N_2 and O_2 (Fig. 3d). The data collected by our wireless micro-probe agreed well with those collected simultaneously using a commercial fibre-optic sensor (NeoFox-GT, FOSPOR-AL300 probe, Ocean Insight) inserted into the same brain region (the bilateral hippocampus, at a depth of ~2.2 mm), suggesting that these systems exhibit a comparable performance (Fig. 3e). We also compared the in vivo performance of our wireless micro-probe with a carbon-based electrochemical electrode[37], which also yielded a similar temporal response (Extended Data Fig. 5). Furthermore, we used the micro-probe to record real-time p_{btO_2} data in mice during acute ischaemia/reperfusion cycles that were induced by clamping and declamping their bilateral carotid arteries (Fig. 3f). The recorded p_{btO_2} levels decreased to less than 3 mm Hg after clamping for about 1 min, and recovered after reperfusion (Fig. 3g). Another validation test monitored and compared the p_{btO_2} levels for mice in awake and anaesthetized states. The micro-probe recorded significantly higher p_{btO_2} levels in mice under isoflurane anaesthesia (Fig. 3h), consistent with previous studies[38]. Finally, and most importantly, the wireless circuit modules supported the acquisition and transportation of data from multiple micro-probes in multiple freely behaving animals, which is a feature scarcely achieved with the tethered fibre-optic system (Fig. 3i and Supplementary Video 1). When supplied with various F_{iO_2} values, the three animals exhibited similar fluctuations in p_{btO_2} (Fig. 3j). These explorations demonstrate the distinct advantages of

https://doi.org/10.1038/s41566-023-01374-y

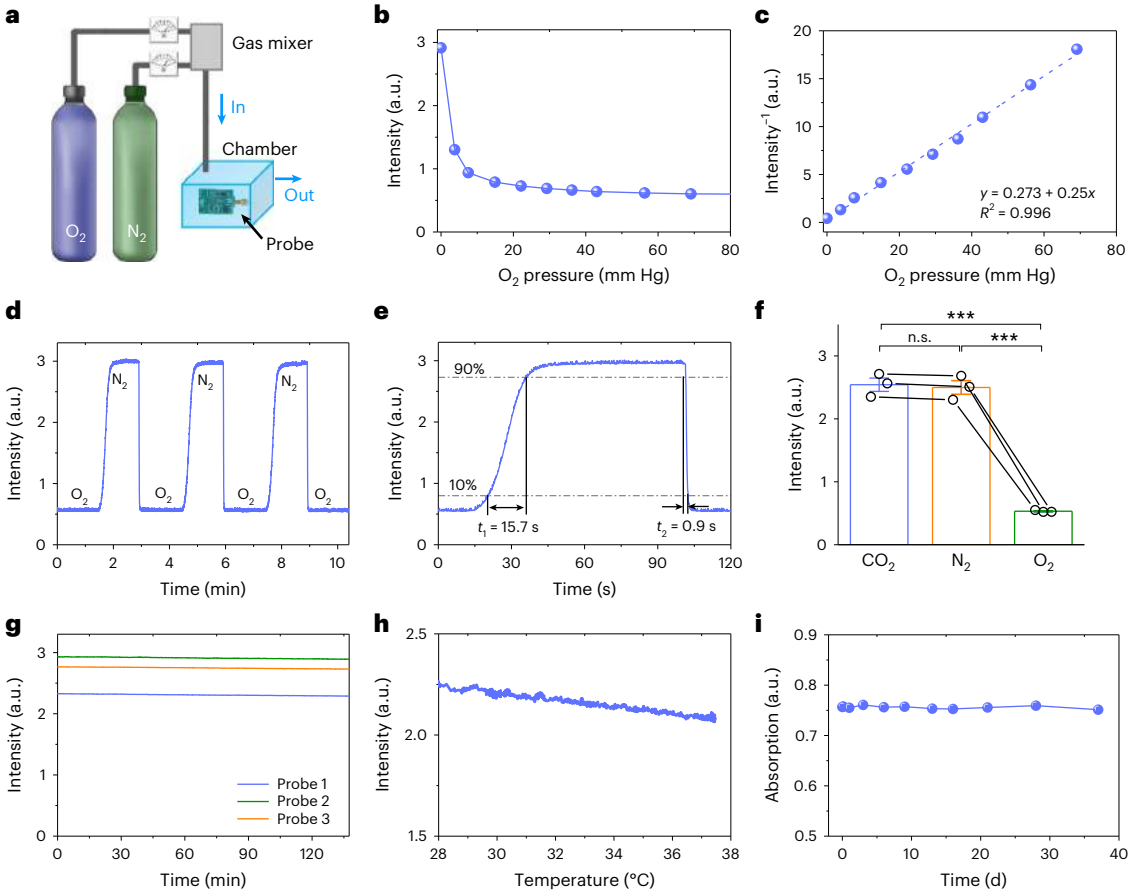

Fig. 2 | In vitro characterization of the p_{btO_2}-sensing probe. a, Illustration of the experimental setup for measuring the probe in response to different concentrations of O_2. The gas chamber has a size of 10 × 10 × 6 cm^3, and the gas flows of N_2 and O_2 are varied. **b**, Recorded PL intensities at different O_2 partial pressures. **c**, Calibration curve showing the linear relationship between the inverse of the PL intensity and the O_2 partial pressure. *R*, coefficient of determination. **d**, Dynamic response of the probe at alternating O_2 partial pressures (from 0 to 760 mm Hg). **e**, Partially enlarged curve of **d**, indicating a rise time t_1 = 15.7 s and a decay time t_2 = 0.9 s. **f**, Recorded signals of the probe responding to different gases (CO_2, N_2 and O_2, at a pressure ~1 atm or ~760 mm Hg). One-way ANOVA (analysis of variance) and LSD (least significant difference) post-hoc comparison are performed (n = 3 probes, ***P < 0.001, n.s. (not significant) P > 0.05). Values are presented as the mean ± s.e.m. **g**, Signal stability of three different probes (LED injection current = 0.5 mA) measured at room temperature in pure N_2. **h**, Probe response at different temperatures (from 28 to 37.5 °C). **i**, Chronic stability of a PtTFPP/PDMS film. The film is immersed in PBS for more than one month and the peak absorption (at 390 nm) is measured on different days.

our wireless micro-probe in studying the real-time p_{btO_2} activities associated with complex animal behaviours and interactions.

Dynamics of p_{btO_2} under hippocampal electrical stimulation

In the mammalian brain, the p_{btO_2} level correlates strongly with local neural activity. Electrical stimulation of the hippocampus can lead to afterdischarges (ADs), and establishes the potential to trigger motor seizures[39]. Intense neural activity usually leads to an increase in local metabolism and O_2 consumption, resulting in a decreased p_{btO_2} level. Utilizing our micro-probe, we investigated local variations in p_{btO_2} in response to electrical stimulation in the deep brain. As shown schematically in Fig. 4a, stimulating and recording electrodes were inserted into the hippocampus (CA1) of the mouse under study. Meanwhile, the optoelectronic micro-probe was implanted into the ipsilateral hippocampus (CA3) to continuously capture changes in p_{btO_2}. The surgical procedures are described in detail in Supplementary Fig. 8. Figure 4b and Supplementary Video 2 display the instance of a dramatic seizure event in a mouse, whose motion behaviours, local field potentials (LFPs) in CA1 and p_{btO_2} levels in CA3 are dynamically monitored simultaneously. In this example, 1-s-long pulsed kindling in CA1 elicits prominent ADs with intensified LFP oscillations and sometimes severe convulsion. The LFP bursts last for about 40 s, and then the micro-probe records a dramatically decreased p_{btO_2} at the end of the animal convulsion, suggesting that intense neural activity causes increased local O_2 consumption. The recorded time-invariant signals at a frequency of 50 Hz (Fig. 4b,e) are associated with the standard alternating current electricity. It is also noted that not every kindling can trigger an AD and associated p_{btO_2} drop, particularly when the time interval between the two stimuli is too short (Supplementary Fig. 9). Statistically, the CA3 region experiences severe hypoxia (p_{btO_2} < 10 mm Hg) approximately 30 s after each AD, and recovers within about 60 s (Fig. 4c). This temporal relationship suggests that the local excessive neural activity leads to more O_2 consumption by the neurons[40], and the resulting hypoxia then suppresses neural activity and terminates the convulsive behaviour in mice[41]. To further understand the O_2 evolution in the tissue, we established a diffusion model based on finite-element analysis (Extended Data Fig. 6). When both the O_2 dissociation from HbO_2 and the O_2 transport are rapid[42], abnormal conditions such as seizures can cause greatly intensified neural activity and excessive O_2 consumption[12], which cannot be fully compensated by the O_2 supply and eventually leads to severe hypoxia.

Furthermore, we utilized the micro-probe to record the p_{btO_2} in a distant region (that is, the contralateral primary motor cortex (M1)) during hippocampal kindling in CA1 (Fig. 4d). As shown in Fig. 4e,f and Supplementary Video 3, the kindling-induced ADs can also elicit

https://doi.org/10.1038/s41566-023-01374-y

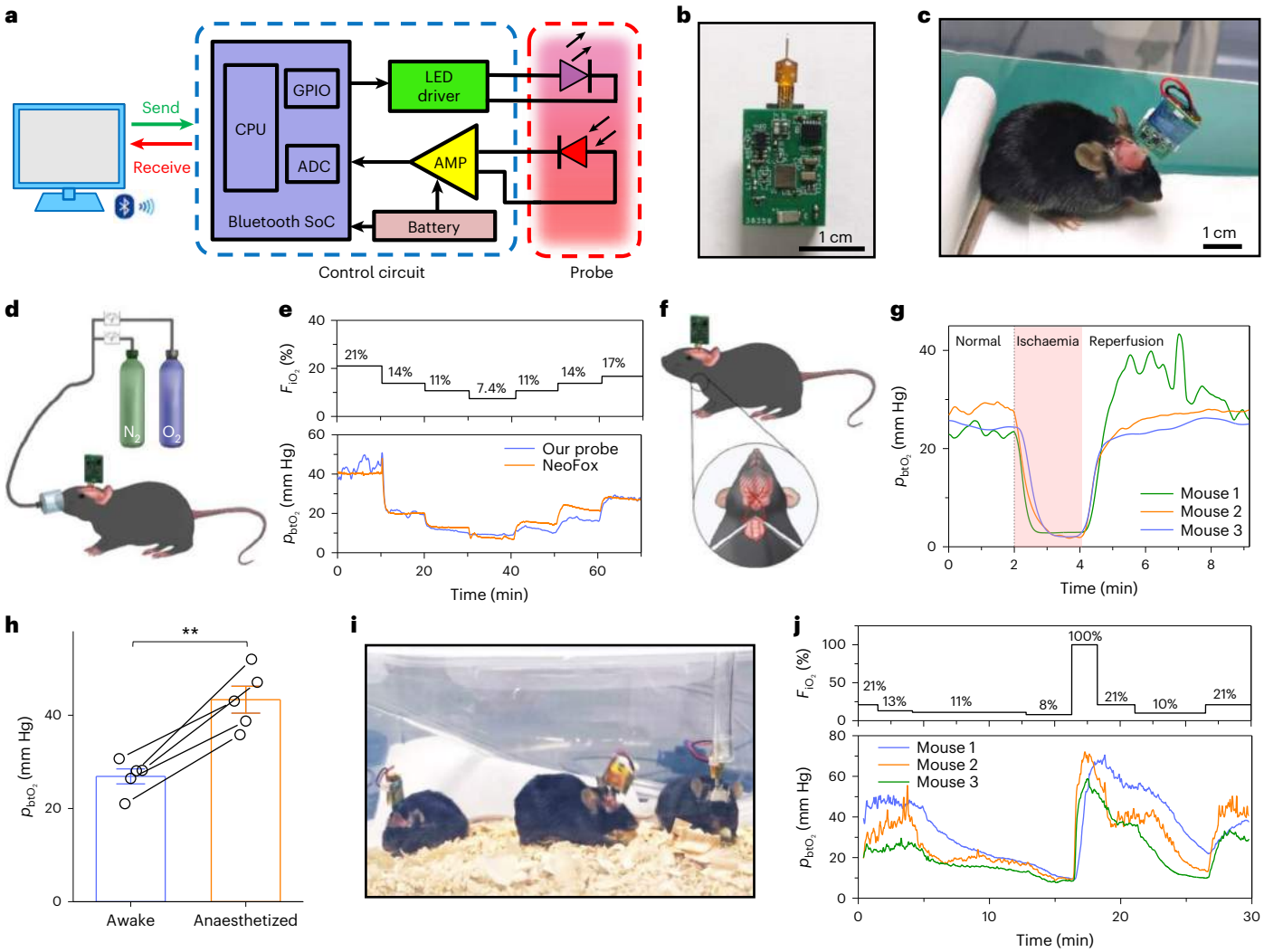

Fig. 3 | The probe combined with a wireless control circuit to continuously monitor p_{btO_2} in the brains of freely behaving mice. a, Block diagram of the wireless system, comprised of a computer, a battery-powered control circuit and an implantable probe. **b**, Image of a probe connected with a wireless circuit. CPU, central processing unit; GPIO, general-purpose input/output port; ADC, analogue-to-digital converter; AMP, operational amplifier; SoC, system on chip. **c**, Photograph showing a freely behaving mouse with an implanted probe and the head-mounted circuit. **d**, Schematic of the setup showing that a wireless probe monitors the p_{btO_2} of a mouse provided with different fractions of inspired O_2 (F_{iO_2}). **e**, Dynamic change in F_{iO_2} (top) and p_{btO_2} results (bottom) detected simultaneously by our wireless probe and a commercial fibre recording system (NeoFox, Ocean Optics). **f**, Schematic showing the probe to monitor the p_{btO_2} of a mouse during acute ischaemia/reperfusion induced by the clamping and declamping of its bilateral carotid arteries. **g**, Recorded p_{btO_2} results during acute ischaemia/reperfusion ($n = 3$ mice). **h**, Comparison of p_{btO_2} results measured for mice in their awake and anaesthetized states. A paired t-test is performed ($n = 5$ mice, $^{**}P < 0.01$, the two-tailed P value is 0.002). Values are presented as the mean ± s.e.m. **i**, Photograph of three freely moving mice with their p_{btO_2} values monitored simultaneously by wireless probes. **j**, Dynamic change in F_{iO_2} (top) and p_{btO_2} results (bottom) that are detected simultaneously in the three mice.

hypoxia in M1. Whereas almost every kindling in CA1 can induce a corresponding hypoxia event in the ipsilateral CA3 region (Fig. 4g), similar p_{btO_2} drops occur in approximately 25% of the trials (16 trials from four mice) (Fig. 4h). Compared with the results in CA3, similar hypoxia events observed in M1 are less pronounced (Fig. 4i) and have a higher latency (Fig. 4j), which may be attributed to the migration of neural activity in the complex brain network[43].

We further examines the blood O_2 saturation in the same region (hippocampus) of the mice, based on the difference in optical absorption between HbO_2 and Hb (Extended Data Fig. 7). Implanted into CA3, optical fibres measured the dynamic change in transmitted light at 660 and 810 nm, determining the S_{tO_2} in the cerebrovascular system (Extended Data Fig. 7a). When varying F_{iO_2}, the dynamic change in recorded S_{tO_2} is similar to that of p_{btO_2} (Extended Data Fig. 7b). Under kindling, however, the responses of these two signals are markedly different (Extended Data Fig. 7c). Whereas our p_{btO_2} probe captures notable hypoxia, the optical fibre records the elevated S_{tO_2} immediately following the stimulation. Such a divergence clearly reveals that S_{tO_2} and p_{btO_2} are two distinct metabolic indicators.

In vivo biocompatibility of the p_{btO_2}-sensing probe

Histological analysis was used to characterize the biocompatibility of the p_{btO_2}-sensing probe in the hippocampal CA3 region of the mice. Through Nissl staining, the coronal section showed the lesion region created by the micro-probe (Supplementary Fig. 10). Results of immunofluorescence staining for glial fibrillary acidic protein (GFAP) at various stages of implantation reveal the astrocyte growth and the fibrosis formation surrounding the lesion region (Extended Data Fig. 8). Immunostaining of vascular endothelial cells (platelet endothelial cell adhesion molecule-1 (CD31)) and antibodies (immunoglobulin G (IgG)) enabled the tissue bleeding condition to be assessed at different stages after probe implantation (Extended Data Fig. 9).

https://doi.org/10.1038/s41566-023-01374-y

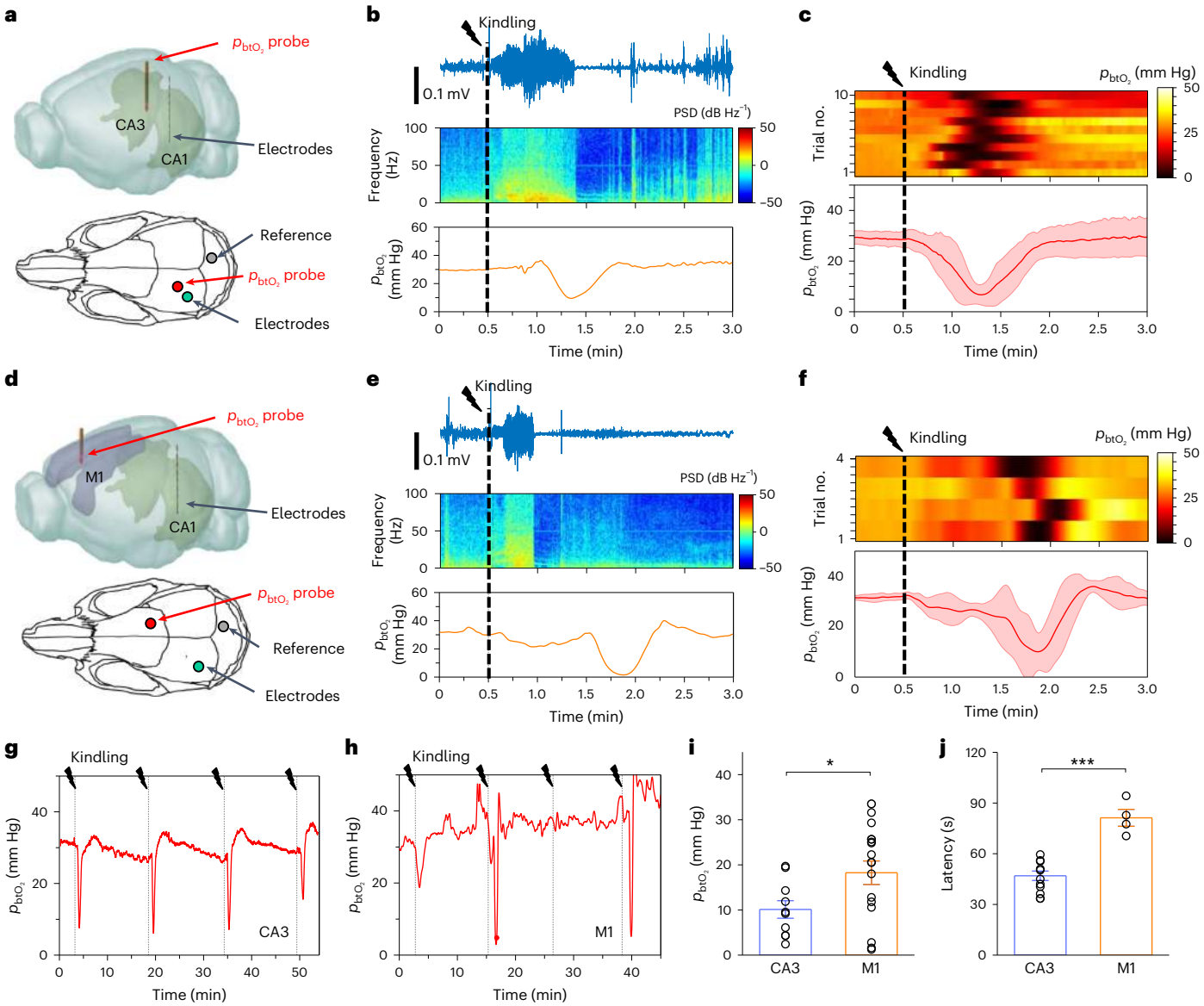

Fig. 4 | Recording of p_{btO_2} signals in different brain regions of mice under electrical stimulation. a, Three-dimensional (3D; upper) and two-dimensional (2D; lower) schematics showing the positions of the p_{btO_2} sensing probe (CA3) and the stimulating/recording electrodes (CA1) implanted in the ipsilateral hippocampus of mice. **b**, Simultaneously recorded electrophysiological activities in CA1 and p_{btO_2} in CA3 under kindling: LFP trace (top); power spectral density (PSD) of the LFP (middle); p_{btO_2} profile (bottom). **c**, Dynamic response of p_{btO_2} recorded in CA3: heatmap of ten individual trials from $n = 10$ mice (top); average p_{btO_2} signals (bottom). The solid lines and shaded areas indicate the mean and s.e.m., respectively. **d**, 3D (upper) and 2D (lower) schematics showing the positions of the p_{btO_2} probe and the electrodes implanted in the contralateral primary motor cortex (M1) and the hippocampus (CA1) of mice. **e**, Simultaneously recorded electrophysiological activities in CA1 and p_{btO_2} in M1 under kindling: LFP trace (top); PSD of the LFP (middle); p_{btO_2} profile (bottom). **f**, Dynamic response of p_{btO_2} recorded in M1: heatmap of four individual trials from $n = 3$ mice (top); average p_{btO_2} signals (bottom). The solid lines and shaded areas indicate the mean and s.e.m., respectively. **g**,**h**, Continuously monitored p_{btO_2} in CA3 (**g**) and M1 (**h**) during sequential kindlings for multiple times. **i**, Comparison of the lowest p_{btO_2} values recorded in the ipsilateral CA3 (ten trials, $n = 5$ mice) and contralateral M1 (16 trials, $n = 4$ mice) regions after kindling in CA1. (*$P < 0.05$, the two-tailed P value is 0.036.) **j**, Comparison of the latency time from kindling in CA1 to reaching the lowest p_{btO_2} in CA3 (ten trials, $n = 5$ mice) and M1 (four trials, $n = 3$ mice). (***$P < 0.001$, the two-tailed P value is 0.000038.) For **i** and **j**, the statistical analysis is based on the t-test of independent samples. Values are presented as mean ± s.e.m.

Moreover, we assessed the chronic operation properties of the micro-probe in vivo (Supplementary Fig. 11). Device degradation and failure occurred after nine days, which was due mainly to water penetration into the tissue. Multilayered inorganic/organic encapsulants will enhance the water resistance of the devices[44]. Further optimizations could involve a reduction of the probe size probe and surface modifications with more biocompatible coatings, such as hydrogels[45], to minimize tissue damage, alleviate fibrosis and mitigate bleeding.

A fully implanted, battery-free probe for p_{btO_2} monitoring

A further technical advance involved the development of a wireless, battery-free circuit module that can be fully implanted subcutaneously, as detailed in Fig. 5a and Supplementary Figs. 12 and 13. Compared with the battery-powered probe, such a battery-free system possesses improved flexibility, reduced weight and longer-lasting data collection without interruption. Protected by a waterproof encapsulant, the entire circuit can be fully implanted under the scalp of freely behaving rats (Fig. 5b,c and Supplementary Fig. 14). X-ray computed tomography

https://doi.org/10.1038/s41566-023-01374-y

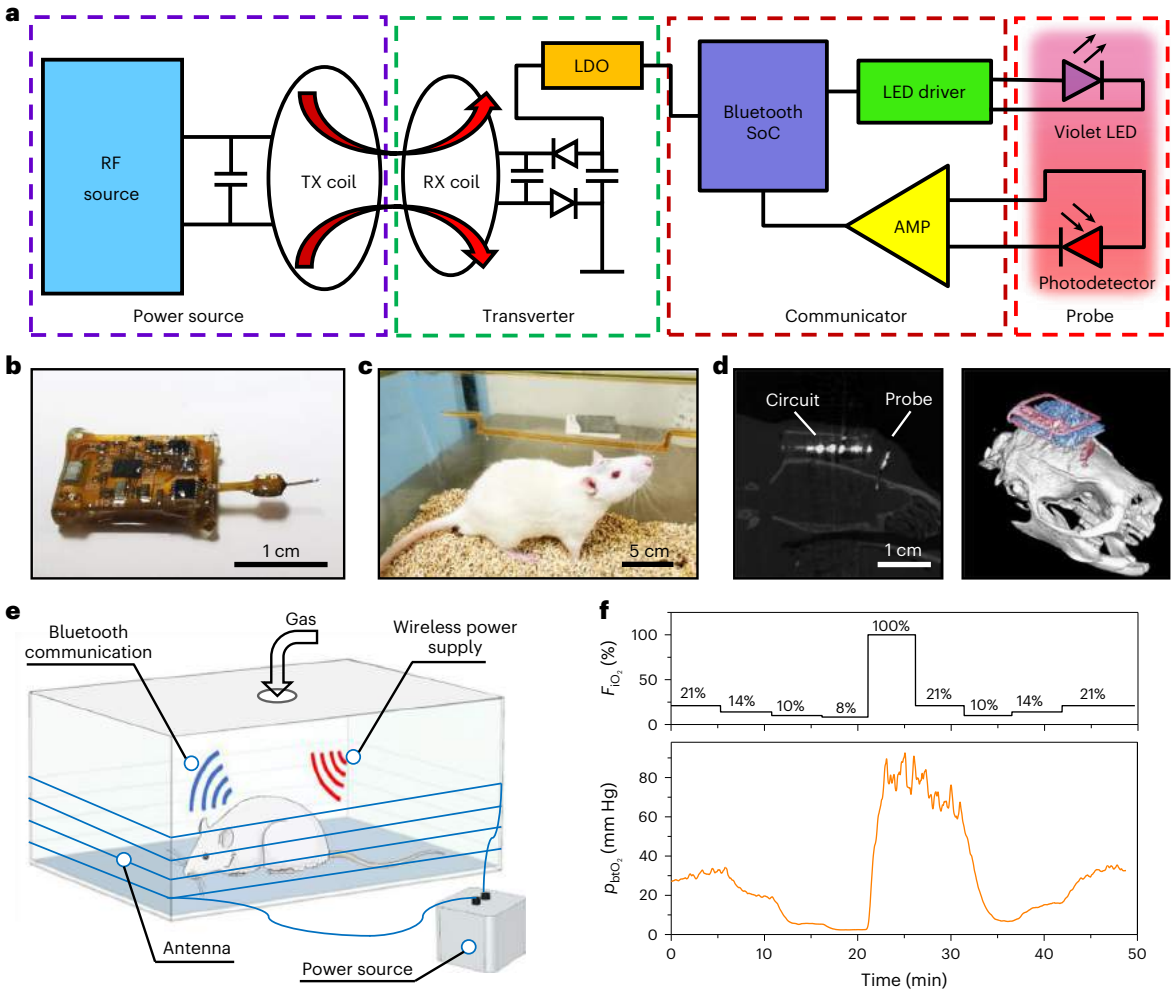

Fig. 5 | A fully implanted, battery-free probe system monitors p_{btO_2} in the brain of living rats. a, Block diagram of the system, which includes an RF power source, a receiving coil, a Bluetooth communication module and an implantable probe. TX, primary coil (transmitted power); RX, secondary coil (received power); LDO, low-dropout regulator. **b**, Image of the probe connected with the battery-free circuit. **c**, Photograph showing a freely moving rat with a fully implanted probe system. **d**, Sagittal CT image indicating the location of the implanted system in a rat (left), and reconstructed 3D CT image showing the position of the device relative to the skull (right). **e**, Schematic illustration of the setup for monitoring p_{btO_2} in rats. **f**, Results of the dynamic change in F_{iO_2} (top) and p_{btO_2} (bottom) monitored in a rat.

(CT) images revealed the location of the p_{btO_2} probe in the rat brain as well as the position of the circuit module (Fig. 5d). As the power transverter, a looped antenna receives currents from an external radio-frequency (RF) source and generates magnetic fields in an enclosure to study the behaviour of the animals (Fig. 5e and Supplementary Fig. 15). Under normal operation, the circuit experienced a temperature rise of less than 3.5 °C, ensuring its safety within the body of the animal (Supplementary Fig. 16). The proof-of-concept study presented in Fig. 5f demonstrates the wireless and continuous monitoring of p_{btO_2} in a rat in response to changes in F_{iO_2} over a period of around 50 min.

Discussion

Supplementary Table 4 compares the characteristics of our micro-probe with those of previous reports. Different from probe systems that sense blood oxygenation (Hb and HbO_2)[15,46], our micro-probe explores cerebral oxygenation through p_{btO_2}. The utilization of a microscale device and a thin-film PtTFPP/PDMS coating guarantees a small tissue lesion and a prompt response (<1 s).

In this study, we monitored the changes in p_{btO_2} induced by electrical stimuli in a seizure model. As a future endeavour, it will be more beneficial to investigate p_{btO_2} before, during and after the occurrence of spontaneous seizures. Although PtTFPP is capable of capturing hypoxic events (p_{btO_2} < 20 mm Hg), its insensitivity at higher O_2 pressures (>20 mm Hg) limits its application in detecting both normal and hyperoxic conditions. In the future, alternative luminophores[47] could be exploited to extend the sensing window to elevated O_2 levels. Our current micro-probe monitors p_{btO_2} in a relatively large brain region (~200 µm) in the hippocampus of mice during ADs that last for tens of seconds. Prospectively, a probe with a much reduced footprint and a faster response would be highly desirable for the detection of more rapid O_2 dynamics in a smaller region or even at the cellular scale.

Besides recording the PL intensity, advanced circuit systems could enable the detection of p_{btO_2} based on PL lifetime changes, which are less susceptible to dye photobleaching and have the potential to provide more accurate measurements[27]. Meanwhile, the combination of electrophysiological activities, p_{btO_2} and blood oxygenation will foster a more profound understanding of neurovascular and neurometabolic coupling. Both battery-powered and battery-free circuit schemes have been introduced for the monitoring of p_{btO_2} in the rodent brain, and they can also be feasible for clinical applications. The two strategies can be combined to realize a stable power supply and wireless charging simultaneously[48,49]. The presented technique clearly indicates its potential utility in neuroscience research and medical diagnostics.

Online content

Any methods, additional references, Nature Portfolio reporting summaries, source data, extended data, supplementary information, acknowledgements, peer review information; details of author contributions and competing interests; and statements of data and code availability are available at https://doi.org/10.1038/s41566-023-01374-y.

References

1. Kaur, C., Foulds, W. S. & Ling, E. Hypoxia-ischemia and retinal ganglion cell damage. *Clin. Ophthalmol.* **2**, 879–889 (2008).
2. Wei, Y., Giunta, S. & Xia, S. Hypoxia in aging and aging-related diseases: mechanism and therapeutic strategies. *Int. J. Mol. Sci.* **23**, 8165 (2022).
3. Ngwenya, L. B., Burke, J. F. & Manley, G. T. Brain tissue oxygen monitoring and the intersection of brain and lung: a comprehensive review. *Respir. Care* **61**, 1232–1244 (2016).
4. Zhang, J. & Piantadosi, C. A. Mitochondrial oxidative stress after carbon monoxide hypoxia in the rat brain. *J. Clin. Invest.* **90**, 1193–1199 (1992).
5. Maloney-Wilensky, E. et al. Brain tissue oxygen and outcome after severe traumatic brain injury: a systematic review. *Crit. Care Med.* **37**, 2057–2063 (2009).
6. Hoffman, W. E. et al. Hypoxic brain tissue following subarachnoid hemorrhage. *Anesthesiology* **92**, 442 (2000).
7. Dombrowski, S. M. et al. Chronic hydrocephalus-induced hypoxia: increased expression of VEGFR-2^{+} and blood vessel density in hippocampus. *Cell. Neurosci.* **152**, 346–359 (2008).
8. Jensen, R. L. Brain tumor hypoxia: tumorigenesis, angiogenesis, imaging, pseudoprogression, and as a therapeutic target. *J. Neurooncol.* **92**, 317–335 (2009).
9. Bateman, L. M., Li, C. S. & Seyal, M. Ictal hypoxemia in localization-related epilepsy: analysis of incidence, severity and risk factors. *Brain* **131**, 3239–3245 (2008).
10. Merelli, A., Repetto, M., Lazarowski, A. & Auzmendi, J. Hypoxia, oxidative stress, and inflammation: three faces of neurodegenerative diseases. *J. Alzheimers Dis.* **82**, S109–S126 (2021).
11. van Santbrink, H., Maas, A. & Avezaat, C. J. Continuous monitoring of partial pressure of brain tissue oxygen in patients with severe head injury. *Neurosurgery* **38**, 21–31 (1996).
12. Özugur, S., Kunz, L. & Straka, H. Relationship between oxygen consumption and neuronal activity in a defined neural circuit. *BMC Biol.* **18**, 76 (2020).
13. Glover, G. H. Overview of functional magnetic resonance imaging. *Neurosurg. Clin. N. Am.* **22**, 133–139 (2011).
14. Sakai, J. Functional near-infrared spectroscopy reveals brain activity on the move. *Proc. Natl Acad. Sci. USA* **119**, e2208729119 (2022).
15. Zhang, H. et al. Wireless, battery-free optoelectronic systems as subdermal implants for local tissue oximetry. *Sci. Adv.* **5**, eaaw0873 (2019).
16. Bai, W. et al. Bioresorbable photonic devices for the spectroscopic characterization of physiological status and neural activity. *Nat. Biomed. Eng.* **3**, 644–654 (2019).
17. Ferrari, M., Mottola, L. & Quaresima, V. Principles, techniques, and limitations of near infrared spectroscopy. *Can. J. Appl. Physiol.* **29**, 463–487 (2004).
18. Toronov, V. et al. The roles of changes in deoxyhemoglobin concentration and regional cerebral blood volume in the fMRI BOLD signal. *Neuroimage* **19**, 1521–1531 (2003).
19. Valadka, A. B., Furuya, Y., Hlatky, R. & Robertson, C. S. Global and regional techniques for monitoring cerebral oxidative metabolism after severe traumatic brain injury. *Neurosurg. Focus* **9**, 1–3 (2000).
20. Gertsenshteyn, I., Giurcanu, M., Vaupel, P. & Halpern, H. Biological validation of electron paramagnetic resonance (EPR) image oxygen thresholds in tissue. *J. Physiol.* **599**, 1759–1767 (2021).
21. Fan, A. P. et al. Quantification of brain oxygen extraction and metabolism with [^{15}O]-gas PET: a technical review in the era of PET/MRI. *Neuroimage* **220**, 117136 (2020).
22. Rivas, L. et al. Micro-needle implantable electrochemical oxygen sensor: ex-vivo and in-vivo studies. *Biosens. Bioelectron.* **153**, 112028 (2020).
23. Marland, J. R. K. et al. Real-time measurement of tumour hypoxia using an implantable microfabricated oxygen sensor. *Sens. Biosensing Res.* **30**, 100375 (2020).
24. Zhou, L. et al. In vivo monitoring of oxygen in rat brain by carbon fiber microelectrode modified with antifouling nanoporous membrane. *Anal. Chem.* **91**, 3645–3651 (2019).
25. Bazzu, G. et al. Real-time monitoring of brain tissue oxygen using a miniaturized biotelemetric device implanted in freely moving rats. *Anal. Chem.* **81**, 2235–2241 (2009).
26. O'Mara, P., Farrell, A., Bones, J. & Twomey, K. Staying alive! Sensors used for monitoring cell health in bioreactors. *Talanta* **176**, 130–139 (2018).
27. Wang, X. D. & Wolfbeis, O. S. Optical methods for sensing and imaging oxygen: materials, spectroscopies and applications. *Chem. Soc. Rev.* **43**, 3666–3761 (2014).
28. Esipova, T. V. et al. Oxyphor 2P: a high-performance probe for deep-tissue longitudinal oxygen imaging. *Cell Metab.* **29**, 736–744.e7 (2019).
29. Davenport, J. J., Hickey, M., Phillips, J. P. & Kyriacou, P. A. Dual pO_2/pCO_2 fibre optic sensing film. *Analyst* **142**, 1711–1719 (2017).
30. Melnikov, P. V. et al. Optical oxygen sensing and Clark electrode: face-to-face in a biosensor case study. *Sensors* **22**, 7626 (2022).
31. Hirakawa, Y. et al. Quantitating intracellular oxygen tension in vivo by phosphorescence lifetime measurement. *Sci. Rep.* **5**, 17838 (2016).
32. Sonmezoglu, S., Fineman, J. R., Maltepe, E. & Maharbiz, M. M. Monitoring deep-tissue oxygenation with a millimeter-scale ultrasonic implant. *Nat. Biotechnol.* **39**, 855–864 (2021).
33. Mao, Y. et al. Highly enhanced sensitivity of optical oxygen sensors using microstructured PtTFPP/PDMS-pillar arrays sensing layer. *Sens. Actuators B* **251**, 495–502 (2017).
34. Lu, L. et al. Wireless optoelectronic photometers for monitoring neuronal dynamics in the deep brain. *Proc. Natl Acad. Sci. USA* **115**, E1374–E1383 (2018).
35. Chu, C.-S. & Lo, Y.-L. High-performance fiber-optic oxygen sensors based on fluorinated xerogels doped with Pt(II) complexes. *Sens. Actuators B* **124**, 376–382 (2007).
36. Suzuki, H., Sugama, A. & Kojima, N. Micromachined Clark oxygen electrode. *Sens. Actuators B* **10**, 91–98 (1993).
37. Xiang, L. et al. Platinized aligned carbon nanotube-sheathed carbon fiber microelectrodes for in vivo amperometric monitoring of oxygen. *Anal. Chem.* **86**, 5017–5023 (2014).
38. Lyons, D. G., Parpaleix, A., Roche, M. & Charpak, S. Mapping oxygen concentration in the awake mouse brain. *eLife* **5**, e12024 (2016).
39. Racine, R., Okujava, V. & Chipashvili, S. Modification of seizure activity by electrical stimulation: III. Mechanisms. *Electroencephalogr. Clin. Neurophysiol.* **32**, 295–299 (1972).
40. Morimoto, K., Fahnestock, M. & Racine, R. J. Kindling and status epilepticus models of epilepsy: rewiring the brain. *Prog. Neurobiol.* **73**, 1–60 (2004).
41. Misonou, H., Mohapatra, D. P., Menegola, M. & Trimmer, J. S. Calcium-and metabolic state-dependent modulation of the voltage-dependent Kv2.1 channel regulates neuronal excitability in response to ischemia. *J. Neurosci.* **25**, 11184–11193 (2005).

42. Popel, A. S. Theory of oxygen transport to tissue. *Crit. Rev. Biomed. Eng.* **17**, 257–321 (1989).
43. Choy, M. et al. Repeated hippocampal seizures lead to brain-wide reorganization of circuits and seizure propagation pathways. *Neuron* **110**, 221–236.e4 (2022).
44. Sang, M., Kim, K., Shin, J. & Yu, K. J. Ultra-thin flexible encapsulating materials for soft bio-integrated electronics. *Adv. Sci.* **9**, 2202980 (2022).
45. Nih, L. R., Sideris, E., Carmichael, S. T. & Segura, T. Injection of microporous annealing particle (MAP) hydrogels in the stroke cavity reduces gliosis and inflammation and promotes NPC migration to the lesion. *Adv. Mater.* **29**, 1606471 (2017).
46. Guo, H. et al. Wireless implantable optical probe for continuous monitoring of oxygen saturation in flaps and organ grafts. *Nat. Commun.* **13**, 3009 (2022).
47. Amao, Y. & Okura, I. Optical oxygen sensing materials: chemisorption film of ruthenium(II) polypyridyl complexes attached to anionic polymer. *Sens. Actuators B* **88**, 162–167 (2003).
48. Kim, C. Y. et al. Soft subdermal implant capable of wireless battery charging and programmable controls for applications in optogenetics. *Nat. Commun.* **12**, 535 (2021).
49. Activa™ RC system (commercial DBS product), *Medtronic* https://www.medtronic.com/us-en/healthcare-professionals/products/neurological/deep-brain-stimulation-systems/activa-platform.html (2022).

Methods

Device fabrication

Details on the device structures and fabrication processes are provided in the Supplementary Information, Supplementary Figs. 1–4 and Supplementary Tables 1 and 2. The InGaP photodetector structure is grown on a GaAs substrate, and the InGaN violet LED structure is grown on sapphire, both via metal–organic chemical vapour deposition. Both the detector and the LED were fabricated using a standard photolithographic process, and freestanding, thin-film microscale devices were formed by selectively etching the $Al_{0.95}Ga_{0.05}As$ sacrificial layer (for the detector)[34] or via ultraviolet laser liftoff (for the LED)[50]. The multilayered silicon dioxide/titanium dioxide longpass filter was deposited onto the GaAs substrate via ion beam-assisted sputtering, with freestanding, thin-film filters formed through femtosecond laser milling and wet etching[51]. A detector, an optical filter and a violet LED were sequentially transferred onto the flexible substrate with PDMS stamps[52], followed by insulation with SU-8 photoresist and metallization. Laser milling (355 nm ultraviolet laser, LPKF ProtoLaser U4) was used to define the needle shape (width ~300 µm, length ~3 mm). Sputtered Cr/Au/Cu/Au layers (6 nm/100 nm/600 nm/150 nm, respectively) served as the interconnect contacts for the devices. Laser milling was used to form the shape of the micro-probes. After encapsulation by PDMS and parylene C, the O_2-sensing film (PtTFPP/PDMS) was dip-coated onto the tip of the probe.

Device characterization and modelling

Characterization of the p_{btO_2}-sensing probe. In vitro characterization of the p_{btO_2}-monitoring probe was carried out using a gas chamber of size 10 × 10 × 6 cm^3, with the gas flow from a gas mixer with two gas flowmeters connected to supplies of pure N_2 (range: ~0–25 litres per min, resolution: 2.5 litres per min) and pure O_2 (range: ~0–1 litres per min, resolution: 0.05 litres per min). The p_{O_2} level was controlled using the two gas flowmeters. Before calibration, the probe underwent photobleaching pretreatment in a pure N_2 environment by supplying the LED with a constant current of 0.5 mA for 30 min. During the in vitro testing, the probe was operated with a sampling frequency of 4 Hz and a driver current of 0.5 mA at a pulse width of 10 ms. The thermal stability testing was performed in a PBS solution containing Na_2SO_3 (5% w/v).

Optoelectronic characterization. The emission spectra of the O_2-sensitive film and the LED were measured with a high-resolution spectrometer (HR 2000+, Ocean Optics). The absorption spectra of the O_2-sensitive film and the transmission spectra of the filter and the PI film were measured using a spectrophotometer (Cary 5000, Agilent Technologies). The current–voltage characteristics of the LED and photodetector were recorded using a Keithley 2400 source meter. The EQE values of the LED and the detector were determined using a spectroradiometer with an integrating sphere (Labsphere). For the in vitro tests, the micro-probes were implanted into a brain phantom made of agarose (0.5% w/v), Hb (0.2% w/v) and a lipid emulsion (Intralipid; 1% w/v) mixed in PBS (98.3% w/v). After stirring, the mixed liquid was heated to boiling, then cooled to room temperature to form a gel.

Optical modelling. A ray-tracing method based on Monte Carlo simulations (TracePro free trial version) was used to simulate the light distribution in the brain. In this model, an LED with a size of 190 × 110 × 10 $µm^3$ emits light at a wavelength of 395 nm, and a detector (185 × 125 × 3 $µm^3$) was placed adjacent to the LED. The LED emission has a Lambertian distribution and was modelled with 1,000,000 rays. A polymer layer with a thickness of 50 µm and a layer of O_2-sensitive film with a thickness of 25 µm were coated onto both devices. The refractive index values of the polymer layer and the O_2-sensitive film are 1.44 at 395 nm and 1.41 at 650 nm, respectively. The O_2-sensitive film has a phosphorescence conversion efficiency of 0.19, a peak molar extinction of 300,000 M^{-1} cm^{-1} and a molar concentration of 0.85 mM. The probe was inserted into the brain tissue (size 5 × 5 × 5 mm^3) with absorption coefficients of 0.75 mm^{-1} and 0.08 mm^{-1}, and scattering coefficients of 30 mm^{-1} and 33 mm^{-1}, for violet (395 nm) and red (650 nm) light, respectively. The tissue had an anisotropy factor of 0.85 and a refractive index of 1.36.

Thermal measurements and modelling. The temperature distributions on the surface of the probe and the circuit board were mapped using an infrared camera (FOTRIC 228). The emissivity values of the probe surface, the surface of the battery-free circuit and the surface of the battery-powered circuit were set to 0.95, 0.95 and 0.80, respectively. A 3D steady-state heat-transfer model was established using finite-element analysis (COMSOL Multiphysics). The materials and the respective corresponding parameters (density, thermal conductivity and heat capacity) used in the model are as follows: parylene (1.11 g cm^{-3}, 0.086 W m^{-1} K^{-1}, 3.5 J g^{-1} K^{-1}), PDMS (0.965 g cm^{-3}, 0.15 W m^{-1} K^{-1}, 1.46 J g^{-1} K^{-1}), PI (1.4 g cm^{-3}, 0.15 W m^{-1} K^{-1}, 1.1 J g^{-1} K^{-1}), Cu (8.96 g cm^{-3}, 400 W m^{-1} K^{-1}, 0.385 J g^{-1} K^{-1}), SU-8 (1.2 g cm^{-3}, 0.2 W m^{-1} K^{-1}, 1.5 J g^{-1} K^{-1}). The boundary condition was natural heat convection to air at 25 °C. The LED served as the heat source, with the input thermal power estimated via $P = V \times I \times (1 - EQE)$, where V, I and EQE are the measured voltage, current and corresponding EQE values for the LEDs. The measured and simulated thermal distribution of the probe surface is shown in Supplementary Fig. 4.

Modelling of O_2 transport. A 2D diffusion model based on the finite-element analysis method (COMSOL Multiphysics) was used to calculate the spatial distribution and the temporal change in p_{O_2} in the brain tissue (Extended Data Fig. 6). The tissue region was of a circular shape with a diameter of 500 µm, in which there were arrays of capillaries with a diameter of 10 µm and a spacing of 50 µm (Extended Data Fig. 6a). The values of p_{O_2} in the capillaries and the tissue outer boundary were fixed to 50 mm Hg and 30 mm Hg, respectively. The dissociation of O_2 from HbO_2 is very rapid and is considered to be instantaneous[42]. Embedded into the tissue, the implantable probe (length 200 µm) comprised a PtTFPP/PDMS-based O_2-sensitive film (thickness 30 µm) and a gas-impermeable substrate (thickness 30 µm). The diffusivities of O_2 in the brain tissue and the PtTFPP/PDMS film are 1.6×10^{-5} cm^2 s^{-1} and 4×10^{-5} cm^2 s^{-1}, respectively[53,54]. The relationship between p_{O_2} and the molar concentration of dissolved O_2 (c_{O_2}) follows Henry's law: $c_{O_2} = p_{O_2} \times \alpha / V_m$, where $\alpha = 0.022$ ml ml^{-1} atm^{-1} is the O_2 solubility in tissue[53] and $V_m = 25.4$ litres per mol is the gas molar volume at 37 °C and 1 atm. During the resting state, the oxygen consumption rate (OCR) was set to 33 µmol $litre^{-1}$ s^{-1} (ref. 55). Enhanced neural activity after kindling is assumed to increase the OCR, with a Gaussian function having a peak six times that of the resting state[12] (Extended Data Fig. 6b, top).

Wireless circuit design

A customized circuit module was designed to operate the LED wirelessly and receive signals from the detector, and a computer or a mobile phone controlled the monitoring system and received the p_{btO_2} signals. The schematic diagram and layout of the printed circuit board for the battery-powered circuit design are depicted in Supplementary Figs. 6 and 7, respectively. A programmable microcontroller (nRF52832, Nordic Semiconductor) was operated at 2.4 GHz for wireless data communication. An LED driver (LTC3212, Analog Devices) with an external resistor supplied a stable current to the LED. The photocurrent of the detector was amplified using an operational amplifier (OPA391, Texas Instruments), and was then digitized by the microcontroller's analogue-to-digital converter for wireless transmission. A linear regulator (NCP161, ON Semiconductor) with a fixed internal output voltage (3.3 V) ensured a stable power supply. The battery-powered circuit had a size of 17.3 × 12.3 mm^2 and a weight of 1.8 g (which included a rechargeable lithium-ion battery with a weight of 1.2 g). The battery had a capacity of 45 mAh and could work continuously for more than eight hours.

The circuit was connected to the implanted probe via a flexible connector. When animals are freely moving, the motion artefact is a major source of noise. The collected raw data were processed via LOWESS (locally weighted scatterplot smoothing) to reduce the high-frequency, zero-mean noise caused by the motion of the animals.

The design of the battery-free circuit was similar to that of the battery-powered circuit, except that it was powered through inductive coupling. The schematic diagram and layout of the fully implanted battery-free circuit are displayed in Supplementary Figs. 12 and 13, respectively. The flexible printed circuit board is based on PI/Cu foils, and an inductive coil with seven turns was used for the power supply. Two capacitors in parallel (~62 pF) were used to tune the power-harvesting antenna. The half-bridge rectifier was made up of two Schottky diodes (Skyworks) and a capacitor (2.2 μF). Located in a cage enclosed by a copper wire antenna with four loops, the p_{btO_2} of the freely behaving rats can be monitored continuously using the fully implanted micro-probe. Electromagnetic finite-element analysis was applied to simulate the magnetic field distribution inside an enclosure measuring 23.0 × 16.0 × 6.5 cm^3 (Supplementary Fig. 15). The antenna was operated at 13.56 MHz, and the output power was 4 W. The maximum temperature rise of the wireless circuit tested at room temperature was less than 3.5 °C (Supplementary Fig. 16).

Biological studies

Animals. All animal procedures were approved by the Institutional Animal Care and Use Committee at Tsinghua University. Adult (8–12-week-old) male wild-type C57BL/6N mice and adult male Sprague–Dawley rats (body weight 350–550 g) purchased from the Vital River Laboratory (Animal Technology) were used and housed in groups (3–5 mice per cage, 1–2 rats per cage) under standard conditions. The animals were maintained on a 12 h light/dark cycle at 22–25 °C and had access to food and water ad libitum.

Stereotaxic surgery. The adult wild-type mice were anaesthetized via an intraperitoneal injection of Avertin (280 mg per kg (body weight)) before surgery and then placed in a standard stereotaxic instrument for surgical implantation. After shaving the scalp and exposing the skull, small holes of ~0.5 mm diameter were drilled in the skull using a micromotor drill. For mice that received electrical stimulation, the p_{btO_2}-sensing probes were implanted slowly in the hippocampus at CA3 (anterior–posterior (AP): −1.8 mm, medial–lateral (ML): ±1.86 mm, dorsal–ventral (DV): −2.25 mm) or M1 (AP: 1.15 mm, ML: 1.7 mm, DV: −2 mm), and a small amount of dental cement was used to fix the probe. For S_{tO_2} sensing, two optical fibres were individually implanted in the hippocampus at an incline (AP: −1.8 mm, ML: 0.7 mm, DV: −1.9 mm, angle: 23°; and AP: −1.8 mm, ML: 2.5 mm, DV: −1.9 mm, angle: 12°). The stimulating/recording electrodes were constructed of twisted Teflon-coated tungsten wires (catalogue no. 796000, A-M Systems) and targeted to the hippocampal CA1 region (AP: −3.0 mm, ML: −2.9 mm, DV: −3.2 mm). A stainless steel screw acted as the reference electrode and was implanted in the skull. Finally, more dental cement was used to fix all devices on the skull (Supplementary Fig. 8).

The battery-free circuit was fully implanted in the Sprague–Dawley rats after they had been anaesthetized via an intraperitoneal injection of mixed Zoletil and xylazine (8 and 15 mg per kg (body weight), respectively). After being placed in a standard stereotaxic instrument for surgical implantation, an incision in the scalp was made to expose the skull. Then, 0.3% hydrogen peroxide was applied to clean the skull, and a small hole with a diameter of ~0.5 mm was drilled. The probe was implanted into the brain (AP: 3.6 mm, ML: 2.0 mm, DV: −2.9 mm), and dental cement was applied to fix the device to the skull followed by suturing of the scalp (Supplementary Fig. 14). To allow the animals to recover, in vivo measurements on the mice and rats were conducted at least four days after surgery.

In vivo p_{btO_2} monitoring. Clamping and declamping of the bilateral carotid arteries was performed on the mice anaesthetized with Avertin (280 mg per kg (body weight)). Under anaesthesia, the wireless circuit was connected to the probe fixed on the mouse skull; the mouse was then placed in a supine position and a small incision was made in the middle of the anterior neck. Next, the muscles under the skin were removed and the bilateral common carotid artery (CCA) was exposed. The left CCA was ligated using a small artery clip, and then the right CCA was ligated. After monitoring for about 2 min, the clips were removed to restore the blood flow.

The micro-probes were used to monitor the p_{btO_2} of freely behaving mice under various F_{iO_2} conditions. One or multiple mice were placed in a gas chamber (size 16.0 × 23.0 × 13.5 cm^3), and the inflowing gas was controlled via two flowmeters connected to pure N_2 and pure O_2. The ratio of the N_2 and O_2 flow rates was varied to achieve different p_{O_2} values.

The p_{btO_2} of the awake mice was measured 5 min after they had been placed the gas chamber with an airflow of 2 litres per min, and their p_{btO_2} in an anaesthetized state was measured after 5 min in flowing air mixed with 2% isoflurane.

Electrical stimulation/kindling was applied to the hippocampal CA1 region of the mice at least four days after surgery. This protocol involved a biphasic pulse train with a current of 0.4 mA, a pulse frequency of 60 Hz and a pulse width of 1 ms, administered for a duration of 1 s. Sequential kindling was applied with a time interval of no less than 10 min for eight times each day until a seizure occurred (usually ~2–4 days after kindling). LFP recording and electrical stimulation were accomplished using an electrophysiological recording system (alphaRS Pro, Alpha Omega Engineering), and the implanted micro-probe simultaneously recorded the p_{btO_2} signals wirelessly.

In vivo S_{tO_2} monitoring. The dynamic S_{tO_2} signals in the hippocampus regions of mice were recorded using a fibre-based setup. A stimulating electrode was implanted in the hippocampal CA1 region, while two fibres (diameter 0.2 mm) were located around the ipsilateral CA3 region. One fibre was coupled to the two LED sources (M660FP1, M810F2, Thorlabs) that emitted alternating red (660 nm) and infrared (810 nm) light (frequency 100 Hz), and the other fibre was coupled to a photodetector (LSSPD-2.5, Beijing Lightsensing Technologies) to receive the signal. The distance between the two fibre ends was about 0.5 mm. The cerebral S_{tO_2}, which is the percentage of HbO_2 (ranging from 0 to 100%), was calculated based on the modified Beer–Lambert law[56]. The normal S_{tO_2} level (baseline) was set to 85%, and the total Hb concentration was set to 2.3 mM. The optical properties of brain tissue and blood were obtained from the literature[57].

Immunofluorescence staining. The mouse brains were fixed with 4% paraformaldehyde (PFA) in PBS and subjected to gradient dehydration, embedded in optimal cutting temperature compound (SAKURA 4583), frozen and sectioned into 10-μm-thick slices using a freezing microtome (Leica 3050S). The sections were incubated with PBS containing 2% bovine serum albumin and 0.5% Triton-X-100 for one hour at room temperature, followed by incubation overnight at 4 °C in PBS containing 2% bovine serum albumin and 0.5% Triton-X-100 with appropriate dilutions of the following primary antibodies: anti-GFAP (ab7260, Abcam; 1:400) and anti-CD31 (AF4709, R&D Systems; 1:40). Then, the sections were washed three times (for 5 min each) at room temperature in PBS, followed by incubation with secondary antibodies (Alexa Fluor 488 donkey anti-goat IgG antibodies: A-11055, 1:1,000; Alexa Fluor 647 donkey anti-rabbit IgG antibodies: A-31573, 1:1,000; Alexa Fluor 555 donkey anti-chicken IgG antibodies: A78949, 1:1,000, all from Thermo Fisher Scientific) for one hour at room temperature. After 5 min in 1:10,000 DAPI (4′,6-diamidino-2-phenylindole) reagent, the sections were washed with PBS again and mounted with coverslips. Images were acquired using a fluorescence microscope (Mica, Leica).

Nissl staining. Mice were anaesthetized with Avertin (280 mg per kg (body weight)) and perfused intracardially with PBS and PFA. The brains were post-fixed in PFA overnight. Coronal brain paraffin sections were taken with a thickness of 5 µm and then deparaffinized with xylene twice (for 20 min each). These sections were rinsed with anhydrous alcohol twice (for 5 min each) and 75% alcohol for 5 min. Then, they were rinsed with tap water and distilled water. After immersion in 0.03% toluidine blue solution (pH = 1.5) for 2–5 min, the samples were washed with tap water. The sections were cleared in xylene for 10 min and mounted using permanent mounting media.

Data availability

The data that support the plots within this paper are available in the Supplementary Information. Source data are provided with this paper.

References

50. Li, L. et al. Heterogeneous integration of microscale GaN light-emitting diodes and their electrical, optical, and thermal characteristics on flexible substrates. *Adv. Mater. Technol.* **3**, 1700239 (2018).
51. Liu, C. et al. High performance, biocompatible dielectric thin-film optical filters integrated with flexible substrates and microscale optoelectronic devices. *Adv. Opt. Mater.* **6**, 1800146 (2018).
52. Carlson, A., Bowen, A. M., Huang, Y., Nuzzo, R. G. & Rogers, J. A. Transfer printing techniques for materials assembly and micro/nanodevice fabrication. *Adv. Mater.* **24**, 5284–5318 (2012).
53. Clark, D. K., Erdmann, W., Halsey, J. H. & Strong, E. in *Oxygen Transport to Tissue — III* (eds Silver, I. A. et al.) 697–704 (Springer, 1978)
54. Charati, S. G. & Stern, S. A. Diffusion of gases in silicone polymers: molecular dynamics simulations. *Macromolecules* **31**, 5529–5535 (1998).
55. Wiesner, H. M. et al. Quantitative and simultaneous measurement of oxygen consumption rates in rat brain and skeletal muscle using ^{17}O MRS imaging at 16.4 T. *Magn. Reson. Med.* **85**, 2232–2246 (2021).
56. Delpy, D. T. et al. Estimation of optical pathlength through tissue from direct time of flight measurement. *Phys. Med. Biol.* **33**, 1433–1442 (1988).
57. Gebhart, S., Lin, W. & Mahadevan-Jansen, A. In vitro determination of normal and neoplastic human brain tissue optical properties using inverse adding–doubling. *Phys. Med. Biol.* **51**, 2011–2027 (2006).

Acknowledgements

This work is supported by the Beijing Municipal Natural Science Foundation (Z220015, to L.Y. and C.W.), the National Natural Science Foundation of China (NSFC) (52272277, to X.S.; 62005016, to H.D.; 8203000638, to G.Z.), the Science and Technology Innovation 2030-Major Project (2021ZD0201801, to G.Z.) and the Beijing Nova Program (20230484254, to H.D.). We thank Dr C. Pan, Prof. P. Yu and Prof. L. Mao for providing carbon-based electrodes for the electrochemical experiments.

Author contributions

X.C., D.S., Z.L., B.Z., G.T., W.Z., Y.X. and X.F. performed the device design, fabrication and characterization. X.C., H.Z., Z.Y., Z.X. and H.D. designed and tested the circuits. X.C., P.W., Q.L., D.S., Y.D., C.W. and Y.W. designed and performed the biological experiments. P.W., C.W., L.Y., H.P., H.D., G.Z. and X.S. provided the tools and supervised the research. X.C., H.D. and X.S. wrote the paper in consultation with the other authors.

Competing interests

The authors declare no competing interests.

Additional information

Extended data is available for this paper at https://doi.org/10.1038/s41566-023-01374-y.

Supplementary information The online version contains supplementary material available at https://doi.org/10.1038/s41566-023-01374-y.

Correspondence and requests for materials should be addressed to He Ding, Guoguang Zhao or Xing Sheng.

Peer review information *Nature Photonics* thanks the anonymous reviewers for their contribution to the peer review of this work.

https://doi.org/10.1038/s41566-023-01374-y

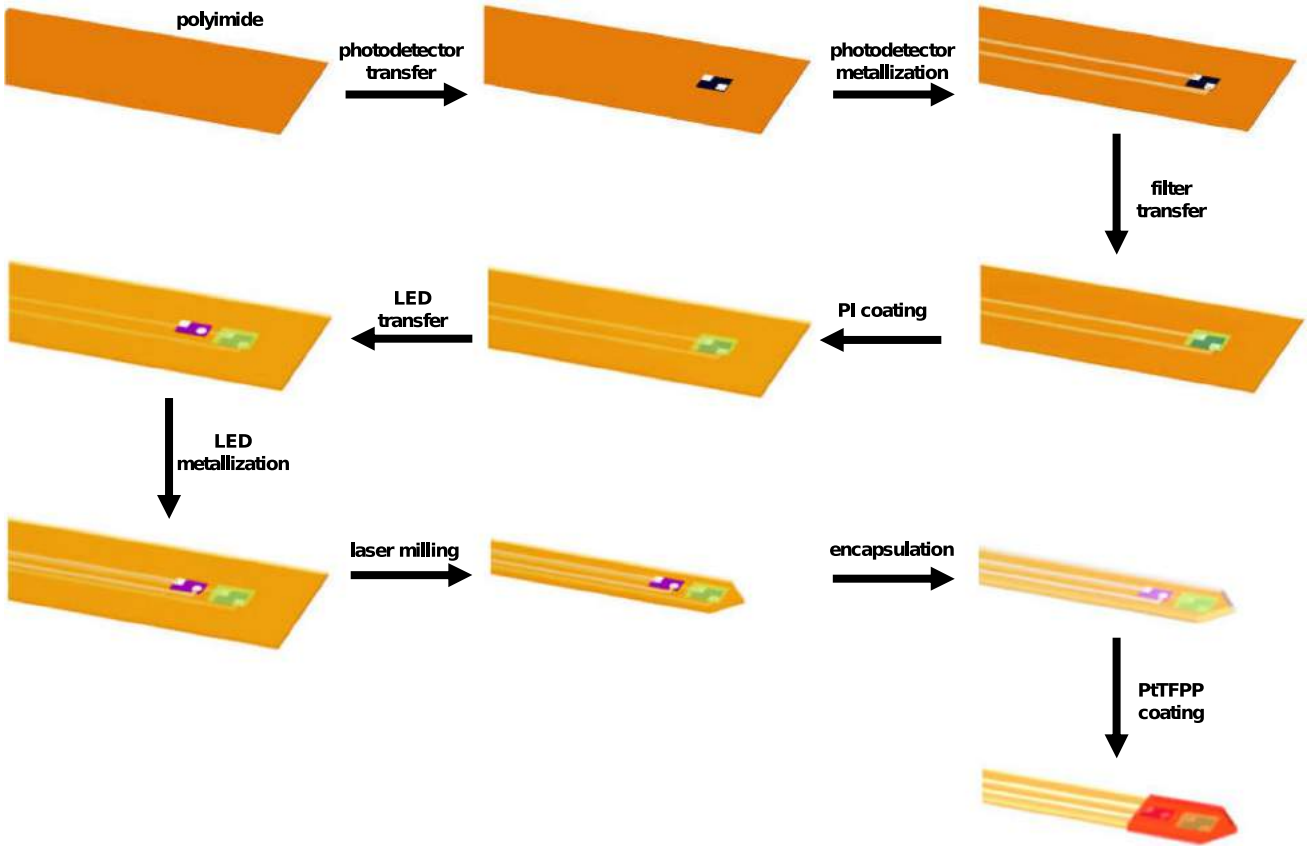

Extended Data Fig. 1 | Schematic illustration of the process flow for fabricating the p_{btO_2} sensing probe.

https://doi.org/10.1038/s41566-023-01374-y

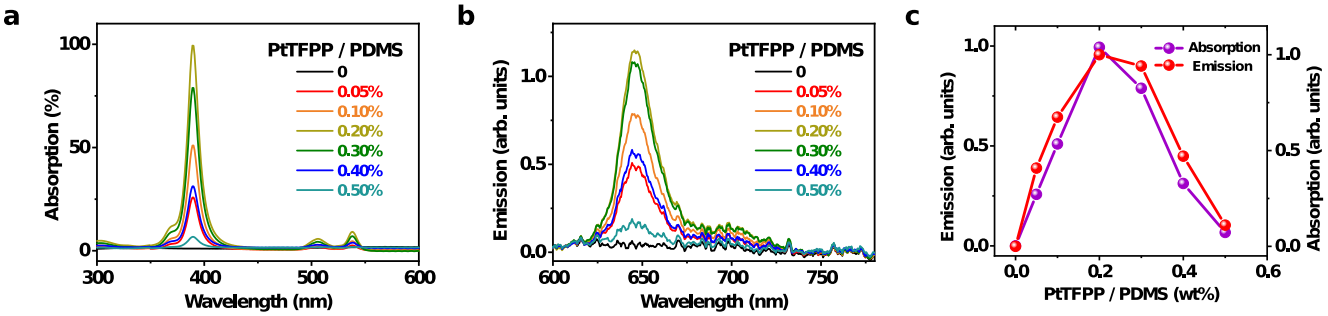

Extended Data Fig. 2 | Optical properties of PtTFPP/PDMS films. (**a**) Absorption and (**b**) PL emission spectra of PtTFPP with different mass concentrations mixed in PDMS films (thickness 10 μm). (**c**) Peak emissions and absorptions as a function of PtTFPP mass concentrations.

https://doi.org/10.1038/s41566-023-01374-y

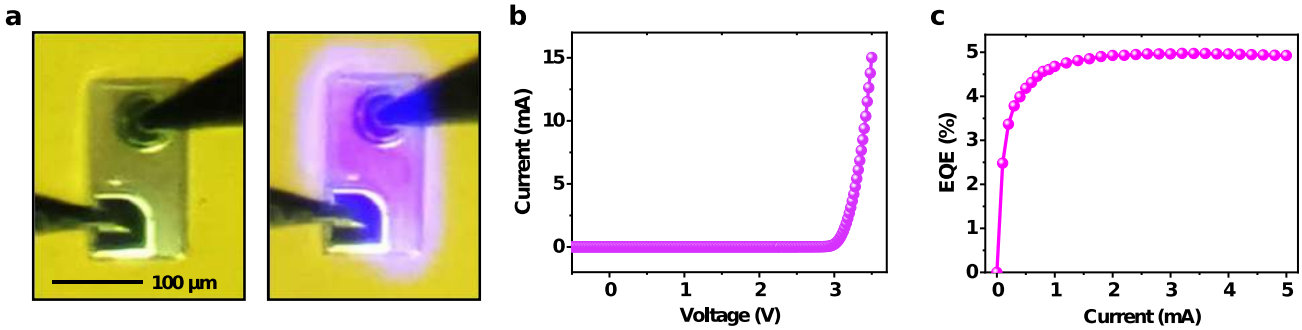

Extended Data Fig. 3 | Images and optoelectronic properties of the InGaN violet LED. (**a**) Microscopic images of a violet LED with (right) and without (left) electroluminescence. (**b**) The LED's current–voltage characteristic curve. (**c**) The LED's external quantum efficiencies (EQEs) as a function of currents.

https://doi.org/10.1038/s41566-023-01374-y

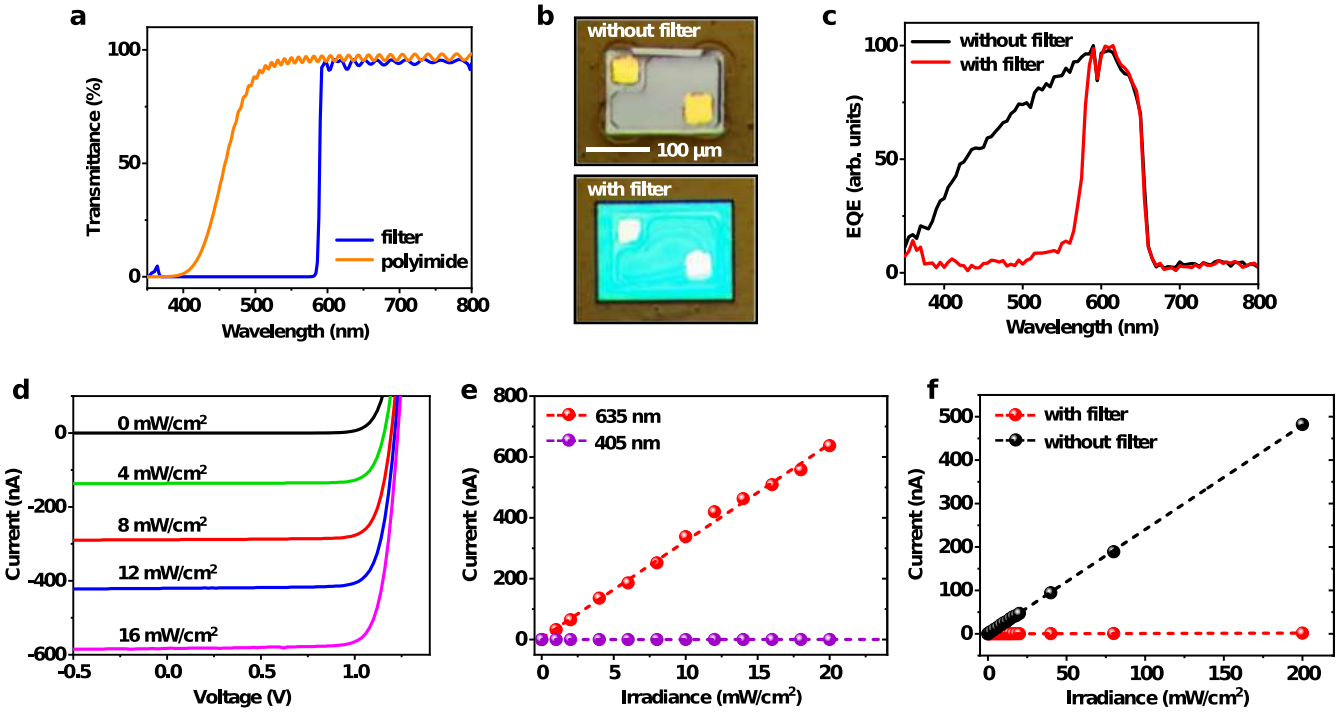

Extended Data Fig. 4 | Images and optoelectronic properties of the InGaP photodetector. (**a**) Transmission spectra of a polyimide film (thickness 8 μm) and a dielectric filter. (**b**) Images of InGaP detectors with (lower) and without (upper) the filter. (**c**) External quantum efficiency (EQE) spectra for InGaP detectors with and without coatings of polyimide and the filter. (**d**) Current–voltage curves of an InGaP detector under different irradiance at 635 nm. (**e**) Photocurrent response of a detector coated with a filter measured at 405 nm and 635 nm illuminations. (**f**) Photocurrent response of a detector with and without filter coatings under 405 nm illumination.

https://doi.org/10.1038/s41566-023-01374-y

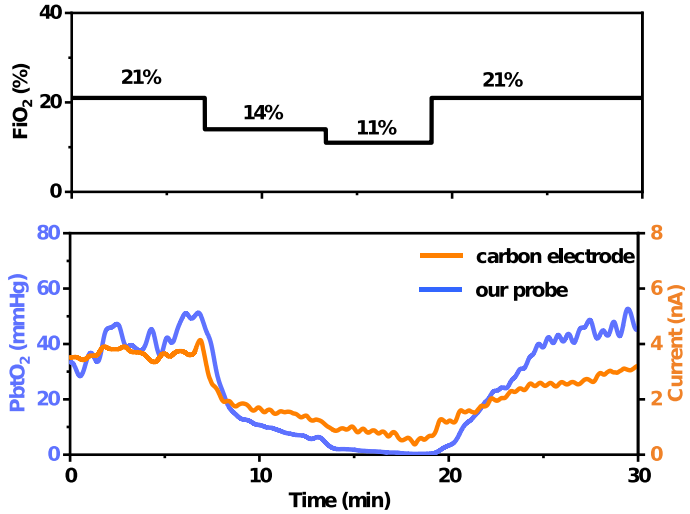

Extended Data Fig. 5 | Dynamic change of F_{iO_2} (top) and p_{btO_2} results (bottom) recorded by our wireless micro-probe, in comparison with the data simultaneously detected by a carbon-based electrochemical electrode[37].

https://doi.org/10.1038/s41566-023-01374-y

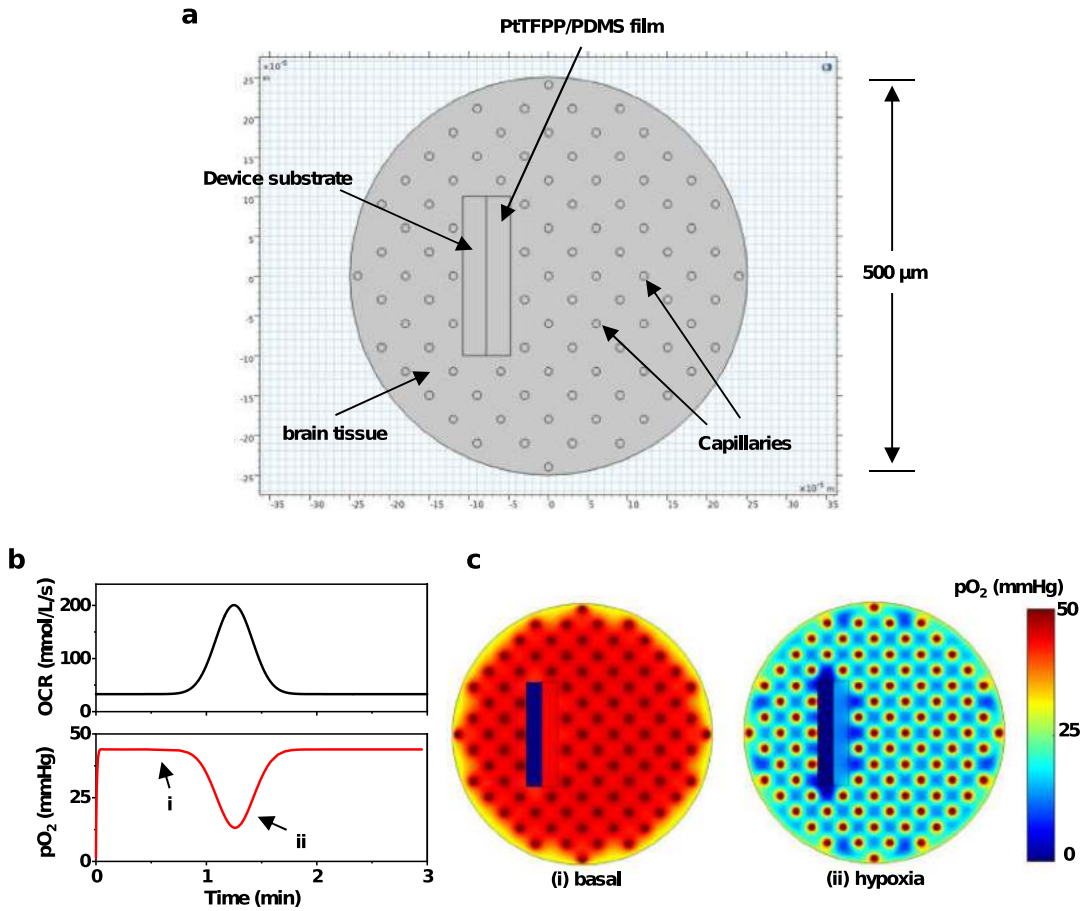

Extended Data Fig. 6 | Numerical simulation of O_2 transport in brain tissue. (**a**) 2D schematic model showing a PtTFPP/PDMS-based oxygen-sensitive film and capillaries within the brain tissue. (**b**) (top) Dynamic oxygen consumption rate (OCR) imported into the model, and (bottom) the corresponding O_2 pressure (p_{O_2}) calculated in the PtTFPP/PDMS film. (**c**) Distributions of p_{O_2} in the tissue during (i) basal and (ii) hypoxia conditions.

https://doi.org/10.1038/s41566-023-01374-y

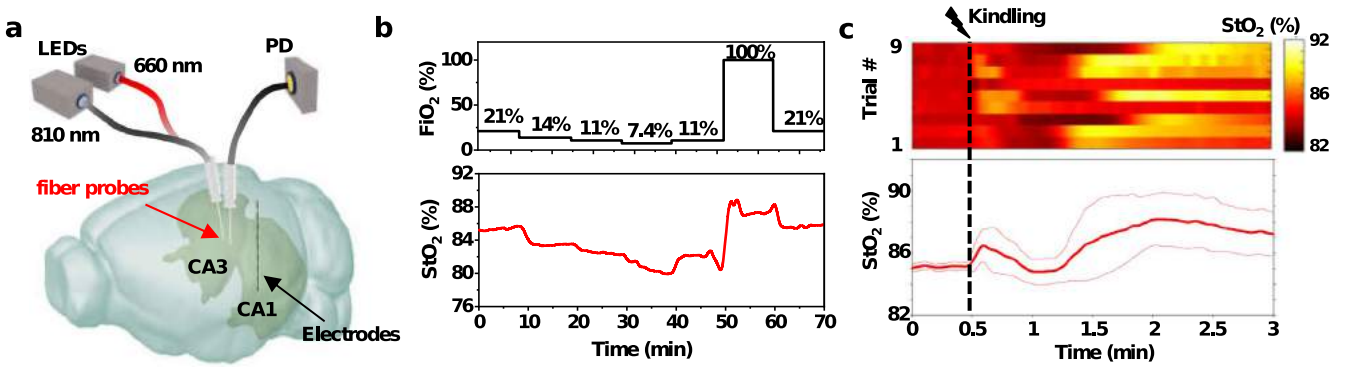

Extended Data Fig. 7 | Measurement of tissue blood oxygen saturation (S_{tO_2}) in the hippocampus of mice using a fibre-based setup. (**a**) 3D schematic model showing positions of the two fibers and the stimulating electrode implanted in the ipsilateral hippocampus of mice (CA3 and CA1, respectively). One fiber couples to two LED sources emitting alternating red (660 nm) and infrared (810 nm) light, and the other couples to a photodetector (PD). (**b**) Dynamic change of F_{iO_2} (top) and corresponding S_{tO_2} results (bottom). (**c**) Dynamic response of S_{tO_2} collected in CA3 immediately after kindling. Top: Heatmap of 9 individual trials from $n = 3$ mice. Bottom: Average StO_2 signals. The solid lines and shaded areas indicate the mean and s.e.m., respectively.

https://doi.org/10.1038/s41566-023-01374-y

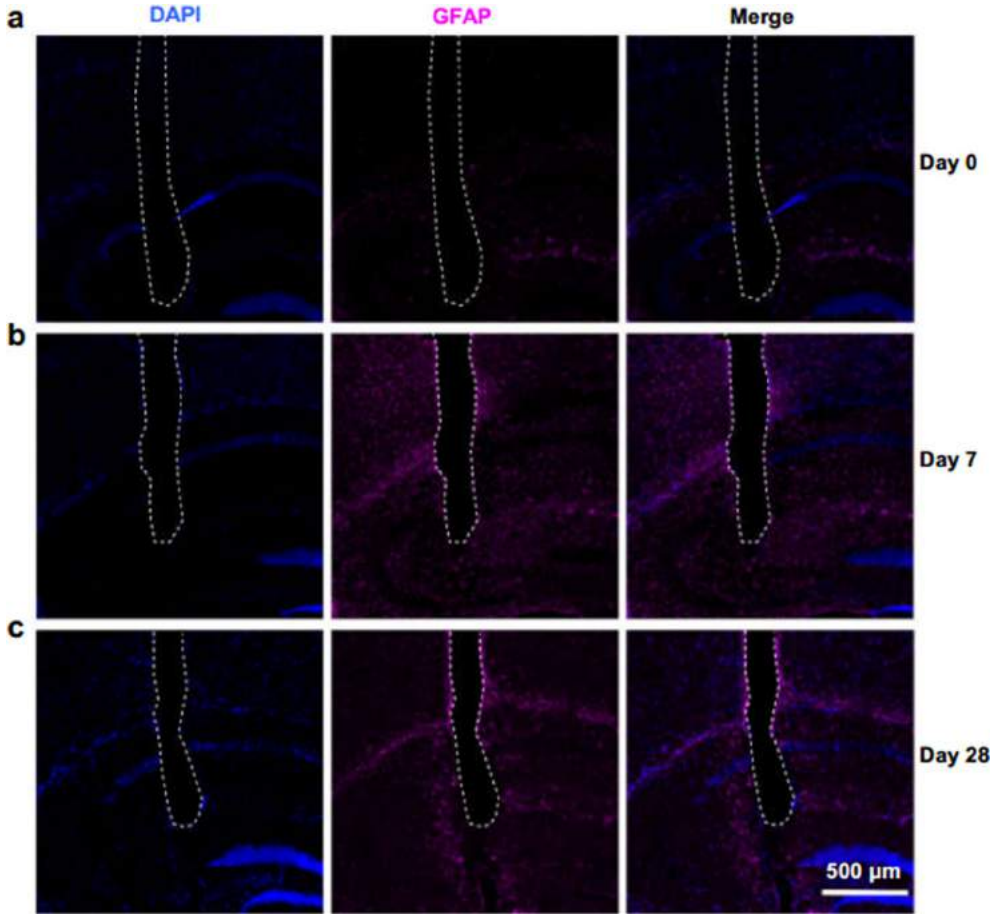

Extended Data Fig. 8 | Representative confocal fluorescence images. showing immunohistochemical staining for nuclei (DAPI, blue), astrocytes (GFAP, purple) and merged images after probe implantation for (**a**) 0, (**b**) 7 and (**c**) 28 days. Lesion areas are outlined by white dashed lines.

https://doi.org/10.1038/s41566-023-01374-y

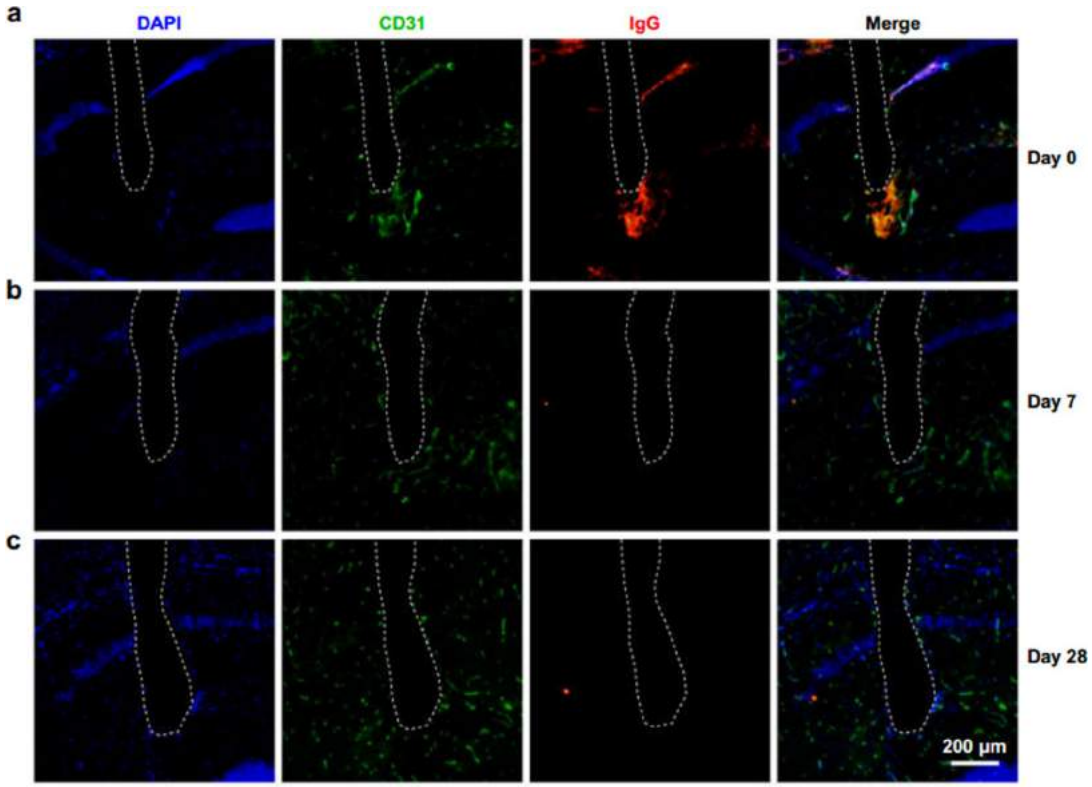

Extended Data Fig. 9 | Representative confocal fluorescence images. showing immunohistochemical staining for DAPI (blue), endothelial cells in blood vessels (CD31, green), immunoglobulin G (IgG, red) and merged images after probe implantation for (**a**) 0, (**b**) 7 and (**c**) 28 days. Lesion areas are outlined by white dashed lines.

nature photonics

Article

https://doi.org/10.1038/s41566-023-01374-y

A wireless optoelectronic probe to monitor oxygenation in deep brain tissue

In the format provided by the authors and unedited

Supplementary Information

Preparation of individual components in the micro-probe

The layout of the microscale oxygen sensing probe includes (from top to bottom) a platinum(II)-5,10,15,20-tetrakis-(2,3,4,5,6-pentafluorophenyl)-porphyrin / poly(dimethylsiloxane) (PtTFPP/PDMS) sensing film (thickness: ~25 μm), a PDMS/parylene C encapsulation layer (thickness: ~50 μm), an SU-8 layer (thickness: 5 μm), an indium gallium nitride (InGaN) violet LED (size: 190 μm × 110 μm × 10 μm), a polyimide (PI) layer (thickness: 8 μm), an optical filter layer based on multilayer titanium dioxide (TiO_2) and silicon dioxide (SiO_2) (size: 220 μm × 150 μm × 6 μm), a PI layer (thickness: ~4 μm) and an indium gallium phosphide (InGaP) photodetector (size: 185 μm × 125 μm × 3 μm), on a copper-clad PI film (Cu/PI/Cu: 18/25/18 μm). Contacts of the LED and the detector are metallized with sputtered metal layers (Cr/Au/Cu/Au = 6 nm/100 nm/600 nm/150 nm).

Fabrication of InGaP detectors

The InGaP detector structure is grown on gallium arsenide (GaAs) substrates via metal-organic chemical vapor deposition (MOCVD). The epitaxially grown stack include (from top to bottom): a 500 nm n-type (Si-doped, 2×10^{18} cm^{-3}) $(Al_{0.7}Ga_{0.3})_{0.5}In_{0.5}P$ filter layer, a 10 nm n-type GaAs (Si-doped, $>6\times10^{18}$ cm^{-3}) top contact layer, a 30 nm n-type (Si-doped, 5×10^{18} cm^{-3}) $In_{0.5}Al_{0.25}Ga_{0.25}P$ window layer, a 100 nm n-type (Si-doped, 2×10^{18} cm^{-3}) $In_{0.5}Ga_{0.5}P$ emitter layer, a 1 μm p-type (Zn-doped, 3×10^{16} cm^{-3}) $In_{0.5}Ga_{0.5}P$ base layer, a 100 nm p-type (Mg-doped, 2×10^{18} cm^{-3}) $In_{0.5}Al_{0.25}Ga_{0.25}P$

back-surface field (BSF) layer, a 100 nm p-type (Mg-doped, $>5\times10^{18}$ cm^{-3}) GaAs contact layer, a 1 μm p-type $In_{0.5}Ga_{0.5}P$ (Mg-doped, 2×10^{18} cm^{-3}) support layer and a 500 nm undoped $Al_{0.95}Ga_{0.05}As$ sacrificial layer on a GaAs substrate (Table S1).

A detailed description of the process to fabricate the freestanding microscale photodetector is listed below:

1. Clean the epi-wafer with acetone, isopropyl alcohol (IPA), and deinoized (DI) water.
2. Dehydrate at 110 °C for 15 min.
3. Spin coat positive photoresist (PR) (SPR220-v3.0, Microchem, 500 rpm / 6 s, 3000 rpm / 30 s) and soft-bake at 110 °C for 1.5 min.
4. Expose PR with a UV lithography tool (URE-2000/25, IOE CAS) with a dose of 300 mJ/cm^2 through a chrome mask, post-bake at 110 °C for 1.5 min.
5. Develop PR in an aqueous base developer (AZ300 MIF), rinse with DI water and hard-bake at 110 °C for 20 min.
6. Etch the $(Al_{0.7}Ga_{0.3})_{0.5}In_{0.5}P$ filter with a mixture of H_3PO_4 and HCl (1:1 by volume) for ~7 s and rinse with DI water.
7. Etch the n-type GaAs contact and the $In_{0.5}Al_{0.25}Ga_{0.25}P$ window with a mixture of H_3PO_4, H_2O_2, and H_2O (3:1:25 by volume) for ~12 s and rinse with DI water.
8. Remove the PR using acetone, IPA and DI water.
9. Dehydrate at 110 °C for 15 min.
10. Spin coat positive photoresist (PR) (SPR220-v3.0, Microchem, 500 rpm / 6 s, 3000 rpm / 30 s) and soft-bake at 110 °C for 1.5 min.

11. Expose PR with UV lithography tools (URE-2000/25, IOE CAS) with a dose of 300 mJ/cm^2 through a chrome mask and post-bake at 110 °C for 1.5 min.
12. Develop PR in aqueous base developer (AZ300 MIF), rinse with DI water and hard-bake at 110 °C for 20 min.
13. Etch the $In_{0.5}Ga_{0.5}P$ emitter, the $In_{0.5}Ga_{0.5}P$ base and the $In_{0.5}Al_{0.25}Ga_{0.25}P$ BSF with concentrated HCl for ~20 s.
14. Remove PR using acetone, IPA, DI water.
15. Dehydrate at 110 °C for 15 min.
16. Spin coat negative photoresist (AZ® nLOF 2070, MicroChemicals, 500 rpm / 6 s, 3000 rpm / 30 s) and soft-bake at 110 °C for 2 min.
17. Expose PR with UV lithography tools (URE-2000/25, IOE CAS) with a dose of 60 mJ/cm^2 through a chrome mask and post-bake at 110 °C for 75 s.
18. Develop PR in aqueous base developer (AZ300 MIF), rinse with DI water.
19. Sputter 6 nm/200 nm of Cr/Au.
20. Lift-off in acetone, and clean the wafer using acetone, IPA, DI water.
21. Dehydrate at 110 °C for 15 min.
22. Pattern PR (SPR220-3.0, Microchem).
23. Etch the p+ GaAs contact in a mixture of $H_3PO_4/H_2O_2/H_2O$ (3:1:25, by volume) for 40 s and rinse with DI water.
24. Etch the $In_{0.5}Ga_{0.5}P$ support and the $Al_{0.95}Ga_{0.05}As$ sacrificial layer with concentrated HCl for ~40 s.
25. Remove the PR using acetone, IPA, DI water.

26. Pattern PR (SPR220-3.0, Microchem).
27. Etch in diluted HF (49% HF : DI water = 1:10, by volume) to release the devices from GaAs growth substrates for ~2.5 h and rinse with DI water.
28. The free-standing InGaP photodetector arrays are formed and ready for picking up.

Fabrication of violet InGaN LEDs

The InGaN based violet LED structures are grown on 2-inch planar sapphire substrates using MOCVD. The main LED structure (from bottom to top) includes: the sapphire substrate, a GaN buffer layer, an n-GaN, an InGaN / GaN multiple-quantum-well (MQW) layer, a p-GaN and an indium tin oxide (ITO) layer for top contacts. The thickness of the entire epitaxial structure is about 10 μm. LED devices are lithographically fabricated, with Cr/Au layers serving as ohmic contacts. Inductively couple plasma reactive ion etching (ICP-RIE) is used to define the LED mesa (lateral dimension 190 μm × 110 μm). After bonding the fully fabricated LED arrays onto a thermal release tape (TRT) (Nitto Denko Corp.), laser lift-off (LLO) is applied to separate the thin-film LEDs from sapphire substrates by thermally decompose GaN into gallium (Ga) metal and nitrogen gas at the interface. A krypton fluoride (KrF) excimer laser at 248 nm (Coherent, Inc., CompexPro110) serves as the light source, with a uniform irradiation area of 5 mm × 15 mm. The power density during LLO is optimized to be around 0.6 J/cm^2 for LEDs. After laser irradiation, the micro-LEDs are released from sapphire by mild mechanical force at 70 °C (melting point of Ga is 29.7 °C). By

heating up to 120 °C, the LEDs are detached from the TRT (the critical release temperature is about 110 °C) and ready for transfer printing by PDMS.

Fabrication of thin-film filters

The filter structure is deposited on a GaAs substrate using ion beam-assisted sputter deposition. The multilayered structure consists of titanium dioxide (TiO_2) and silicon dioxide (SiO_2) films with a total thickness of about 6.6 μm. Its detailed layer structure can be found in our previous work[1]. Its shape (size: 220 μm × 150 μm) is defined through femtosecond laser-cutting (800 nm, Ti-sapphire laser system, Coherent Inc.). Subsequently, the GaAs substrate is removed in a mixed solution with NH_4OH, H_2O_2 and H_2O (1:1:2, by volume) for ~8 hours. Finally, PDMS stamps (Sylgard 184 from Dow Corning) are utilized to transfer and print the freestanding thin-film filters onto other foreign substrates.

Synthesis of the PtTFPP/PDMS film

To fabricate the oxygen-sensitive film, commercial platinum(II)-5,10,15,20-tetrakis-(2,3,4,5,6-pentafluorophenyl)-porphyrin (PtTFPP) powders (PtT975, Frontier Scientific) are dissolved in toluene (0.08 mol/L), followed by the addition of the base component (part A) of polydimethylsiloxane (PDMS) to the solution, with different PtTFPP: PDMS weight ratios (0–0.50 wt%). After evaporating the solvent overnight, the substance is mixed with curing agent (part B) of PDMS with a weight ratio of 10:1

(part A/part B). Subsequently, vacuum evacuation removes air bubbles. The PtTFPP/PDMS film is ready for dip coating on the optoelectronic micro-probe.

Preparation of the adhesive solution

The adhesive solution comprises: bisphenol A glycerolate (1 glycerol/phenol) diacrylate, 3-(Trimethoxysilyl) propyl methacrylate, spin-on-glass (SOG 500F, Filmtronics Inc.), 2-Benzyl-2-(dimethylamino)-4'-morpholinobutyrophenone, and anhydrous ethanol[2]. The weight ratio is 200:100:100:9:2000. Stir at room temperature until full mixing. Store the mixed solution in refrigerator (4 °C) for future use.

Fabrication of the microscale optoelectronic probe

A detailed description of the fabrication process is listed below:

Substrate preparation

1. Cut the copper-clad PI substrate (Cu/PI/Cu: 18/25/18 μm, DuPont) into small pieces (size: 15 mm × 18 mm).
2. Laminate the copper-clad polyimide film onto a PDMS coated glass slide
    a. Degas PDMS (Sylgard 184) 10 : 1 (base: curing agent, by weight).
    b. Spin cast PDMS to a glass slide at 500 rpm/6 s, 3000 rpm/30 s to form a PDMS film (thickness: ~10 μm).
    c. Bake the glass for 23 s at 110 °C.
    d. Laminate the PI film onto the PDMS coated glass. Make sure that the polyimide attaches to PDMS tightly without any bubbles.
    e. Bake the sample for 30 mins at 110 °C until PDMS is fully cured.
    f. Clean the sample by acetone, IPA and DI water.
    g. Dehydrate at 110 °C for 15 min.
    h. Spin cast 8 μm polyimide (YDPI-102, Jing'ai Microelectronics) at 500 rpm/9 s, 3000 rpm/30 s to form an insulating film.
    i. Bake the sample for 1 h at 80 °C, 1 h at 130 °C, 1 h at 180 °C, 3 h at 230 °C.

InGaP detector transfer

3. Clean the PI sample by acetone, IPA and DI water.

4. Dehydrate at 110 °C for 15 min.
5. Spin coat negative photoresist (PR) (AZ nLOF 2070, 500 rpm / 6 s, 3000 rpm / 30 s) and soft-bake at 110 °C for 2 minutes 20 seconds.
6. Expose PR with UV lithography tools (URE-2000/25, IOE CAS) with a dose of 60 mJ/cm^2 (URE-2000/25, IOE CAS) through a chrome mask and post-exposure bake at 110 °C for 75 s.
7. Develop PR in an aqueous base developer (AZ300 MIF) and rinse with DI water.
8. Deposit 50 nm Al as the markers by sputtering.
9. Lift off PR in acetone.
10. Clean the substrate and dehydrate at 110 °C for 10 min.
11. Spin coat the prepared adhesive solution (500 rpm/6 s, 3000 rpm/30 s) on the substrate and soft-bake at 110 °C for 3 mins.
12. Transfer print InGaP detectors from the source GaAs wafer onto the processed substrate with PDMS stamps.
13. Cure under UV for 10 minutes and bake at 110 °C for 3 h.
14. Clean the PR by reactive ion etching (RIE) (O_2, 200 sccm, 90 mTorr, 150 W) for 12 min.

InGaP detector encapsulation

15. Clean the sample (acetone, IPA, DI water) and dehydrate at 110 °C for 15 min.
16. Clean by RIE (O_2, 200 sccm, 90 mTorr, 150 W) for 1 min.
17. Spin coat SU8-3005 epoxy (500 rpm/6 s, 3000 rpm/30 s).
18. Soft-bake at 65 °C for 1 min and 95 °C for 3 min.

19. Pattern SU8 to expose contact pads of the detector by UV lithography with a dose of 210 mJ/cm^2.
20. Post-bake at 65 °C for 1 min and 95 °C for 2 min.
21. Develop in propylene glycol monomethyl ether acetate (PGMEA) for 2.5 min and rinse with IPA.
22. Hard bake at 130 °C for 2h.

InGaP detector metallization

23. Clean the sample (acetone, IPA, DI water) and dehydrate at 110 °C for 15 min.
24. Pattern PR AZ nLOF 2070.
25. Deposit Cr/Au/Cu/Au = 6 nm/100 nm/600 nm/150 nm by sputtering.
26. Lift-off PR in acetone.

Filter transfer

27. Clean the sample (acetone, IPA, DI water) and dehydrate at 110 °C for 15 min.
28. Spin coat 2 μm polyimide (500 rpm/6 s, 3000 rpm/30 s) and bake at 110 °C for 2 h.
29. Spin coat 2 μm polyimide (500 rpm/6 s, 3000 rpm/30 s).
30. Bake at 85 °C for 10 s.
31. Transfer print dielectric filters on top of detectors with PDMS stamps.
32. Hard-bake at 110 °C for 2 h.

InGaN LED transfer

33. Clean the sample (acetone, IPA, DI water) and dehydrate at 110 °C for 15 min.
34. Spin coat 8 μm polyimide (500 rpm/6 s, 3000 rpm/30 s).

35. Bake at 85 °C for 2 min.
36. Transfer print InGaN violet LEDs onto the substrate with PDMS stamps.
37. Hard-bake at 85 °C for 1 h and 130 °C for 4 h.

InGaN LED encapsulation

38. Clean the sample (acetone, IPA, DI water) and dehydrate at 110 °C for 15 min.
39. Clean by RIE (O_2, 200 sccm, 90 mTorr, 150 W) for 1 min.
40. Spin coat SU8-3005 epoxy (500 rpm/6 s, 3000 rpm/30 s).
41. Soft-bake at 65 °C for 1 min and 95 °C for 3 min.
42. Pattern SU8 to expose contact pads of the LED by UV lithography with a dose of 210 mJ/cm^2.
43. Post-bake at 65 °C for 1 min and 95 °C for 2 min.
44. Develop in PGMEA for 2.5 min and rinse with IPA.
45. Hard bake at 130 °C for 2h.

InGaN LED metallization

46. Clean the sample (acetone, IPA, DI water) and dehydrate at 110 °C for 15 min.
47. Pattern PR AZ nLOF 2070.
48. Deposit Cr/Au/Cu/Au = 6 nm/100 nm/600 nm/150 nm by sputtering.
49. Lift-off PR in acetone.

Device encapsulation

50. Clean the sample (acetone, IPA, DI water) and dehydrate at 110 °C for 15 min.
51. Expose under ultraviolet induced ozone (UV Ozone, PCE-22-LD, YIMA) for 15 min.

52. Pattern SU8-3005 epoxy (500 rpm / 5 s, 3000 rpm / 30 s), cure under UV for 210 mJ / cm^2 and bake at 110 °C for 30 min.

Laser milling

53. Use laser milling to cut the PI film into micro-probe shapes (LPKF ProtoLaser U4, 365 nm; 1000 Hz, 0.5 W, 50 repeats + 1 W, 100 repeats + 2W, 40 repeats)

Device encapsulation

54. Expose the micro-probes under UV ozone for 15 min.
55. Encapsulate the micro-probes with PDMS
    a. Degas PDMS 10:1 (base: curing agent, by weight).
    b. Dip coat the micro-probes with PDMS.
    c. Bake the probes in 75 °C for 2 h.
56. Coat the probes with a layer of parylene C (14 μm, Specialty Coating Systems).
57. Clean the probes with RIE (O_2, 200 sccm, 90 mTorr, 150 W) for 1 min.
58. Encapsulate the probes with another layer of PDMS.
59. Dip the synthesized PtTFPP/PDMS on the tip of the probe.

References

1. Li L, Tang G, Shi Z, Ding H, Liu C, Cheng D, et al. Transfer-printed, tandem microscale light-emitting diodes for full-color displays. Proceedings of the National Academy of Sciences 2021, 118(18): e2023436118.

2. Kim T-i, Kim MJ, Jung YH, Jang H, Dagdeviren C, Pao HA, et al. Thin film receiver materials for deterministic assembly by transfer printing. Chemistry of Materials 2014, 26(11): 3502-3507.

Figure S1

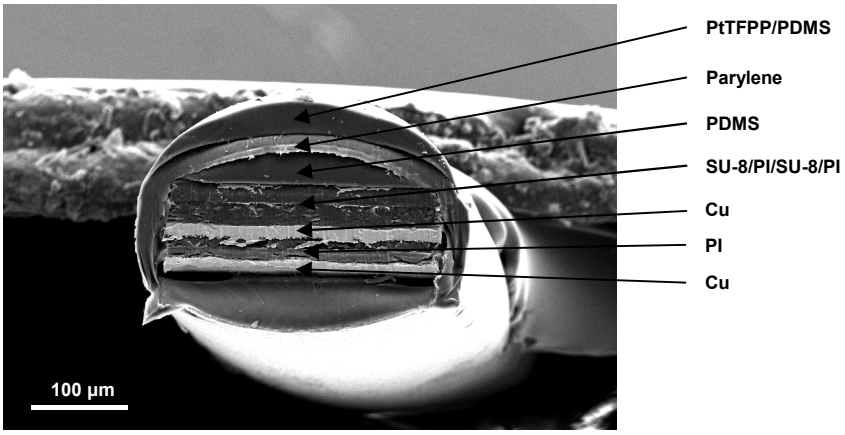

Figure S1. SEM image (cross-sectional view) of the probe with encapsulation layers.

Figure S2

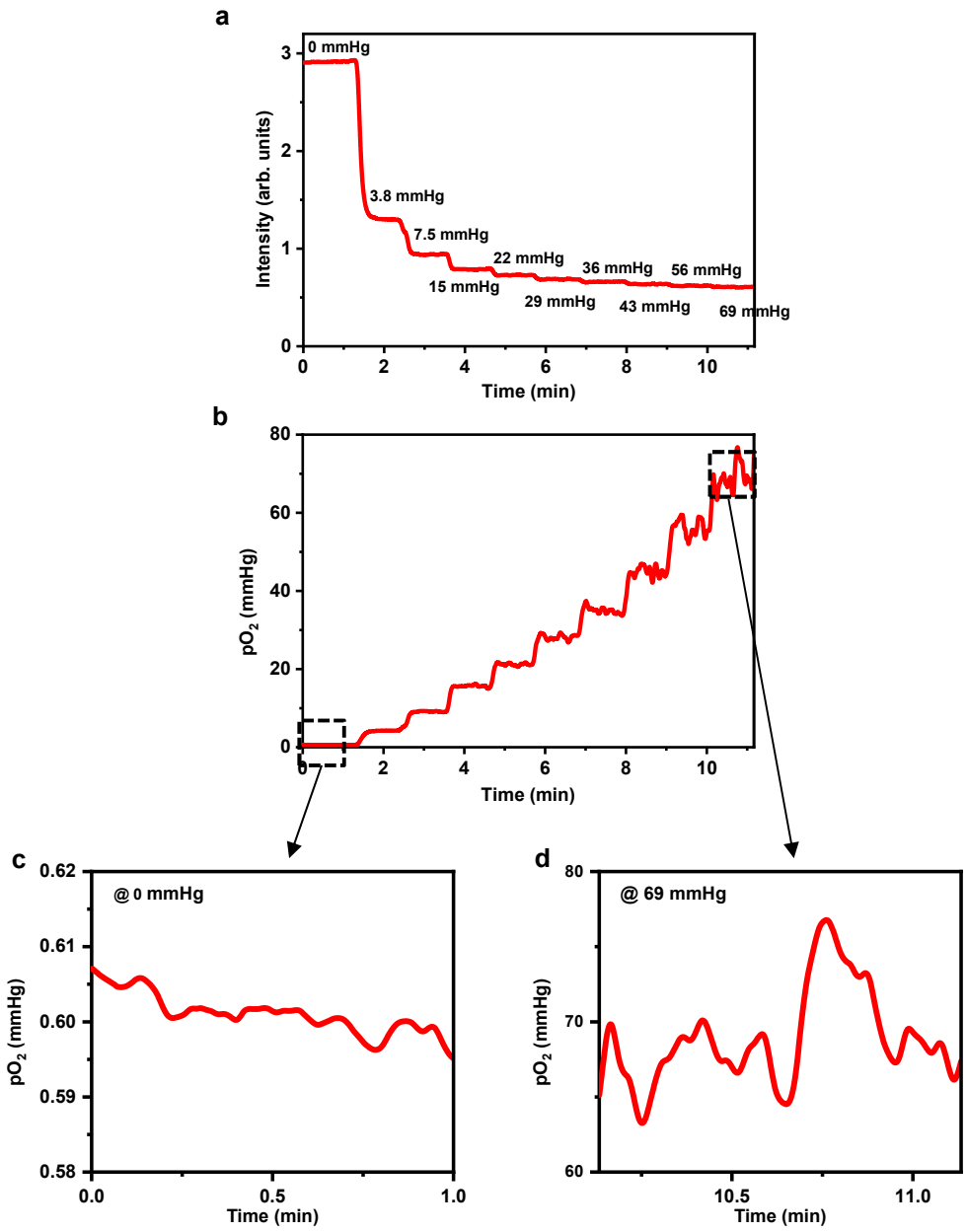

Figure S2. (a) Recorded PL intensities at different O_2 partial pressures changing with time. (b) Calibrated O_2 partial pressures with time based on the Stern-Volmer equation. (c, d) Partially enlarged curve of (b) at (c) 0 mmHg and (d) 69 mmHg.

Figure S3

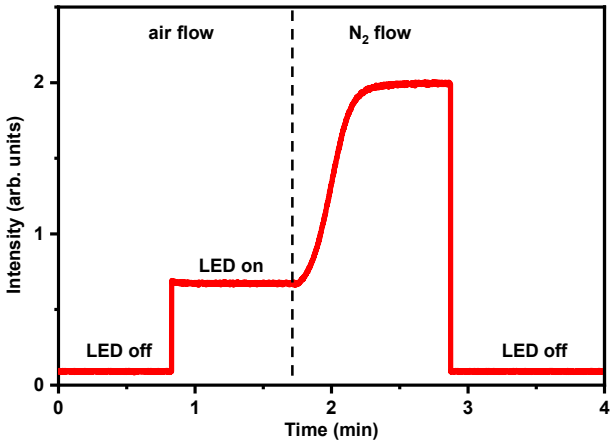

Figure S3. Composition of the recorded signal. The initial value of the signal collected by the circuit is set to 0.1 to enable the amplifier to operate within its linear range. When the LED is on, the signal in air (~0.5) mainly comes from the excitation violet light, which cannot be completely blocked by the filter and leaks into the detector. When N_2 is filled into the chamber, phosphorescence becomes stronger, which can be used to calculate $PbtO_2$.

Figure S4

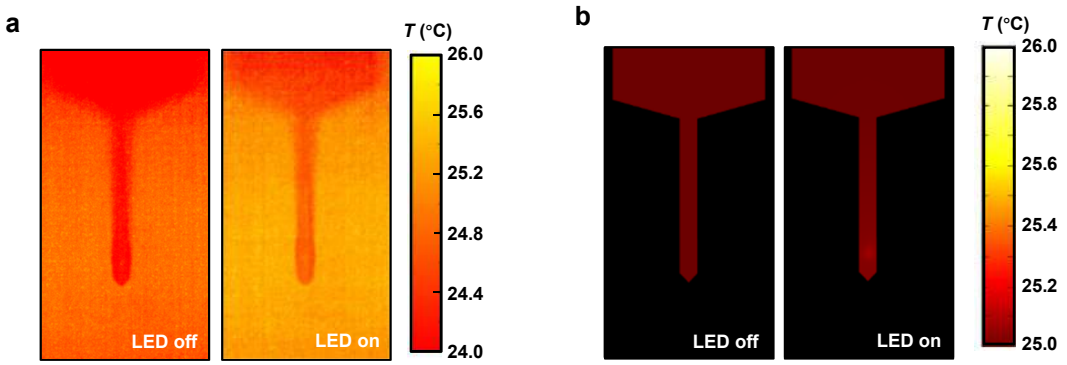

Figure S4. Thermal properties of the probe. (a) Measured and (b) simulated temperature distributions on the probe surface when the violet LED is off (left) or on (right) in air (LED current 0.5 mA, frequency 4 Hz, duty cycle 5%).

Figure S5

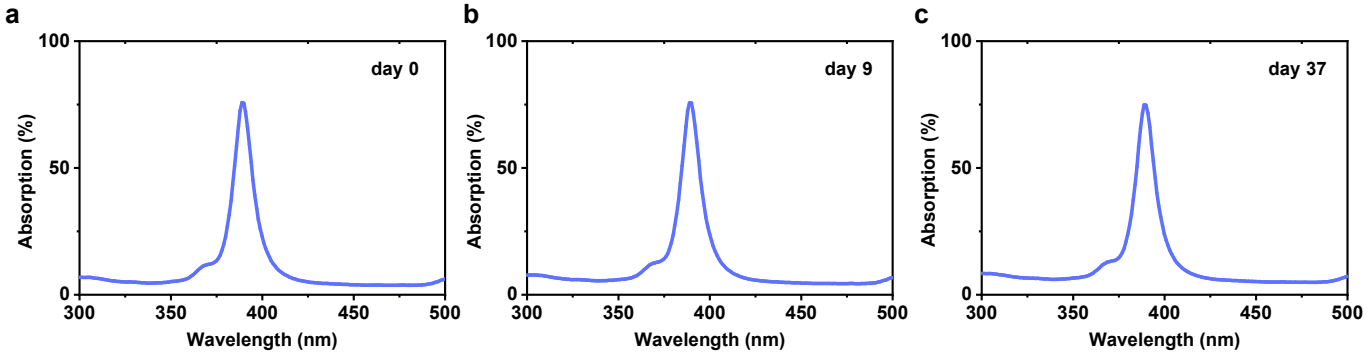

Figure S5. Absorption spectra of the oxygen sensing film immersing the film in PBS for 0 day (a), 9 days (b) and 37 days (c).

Figure S6

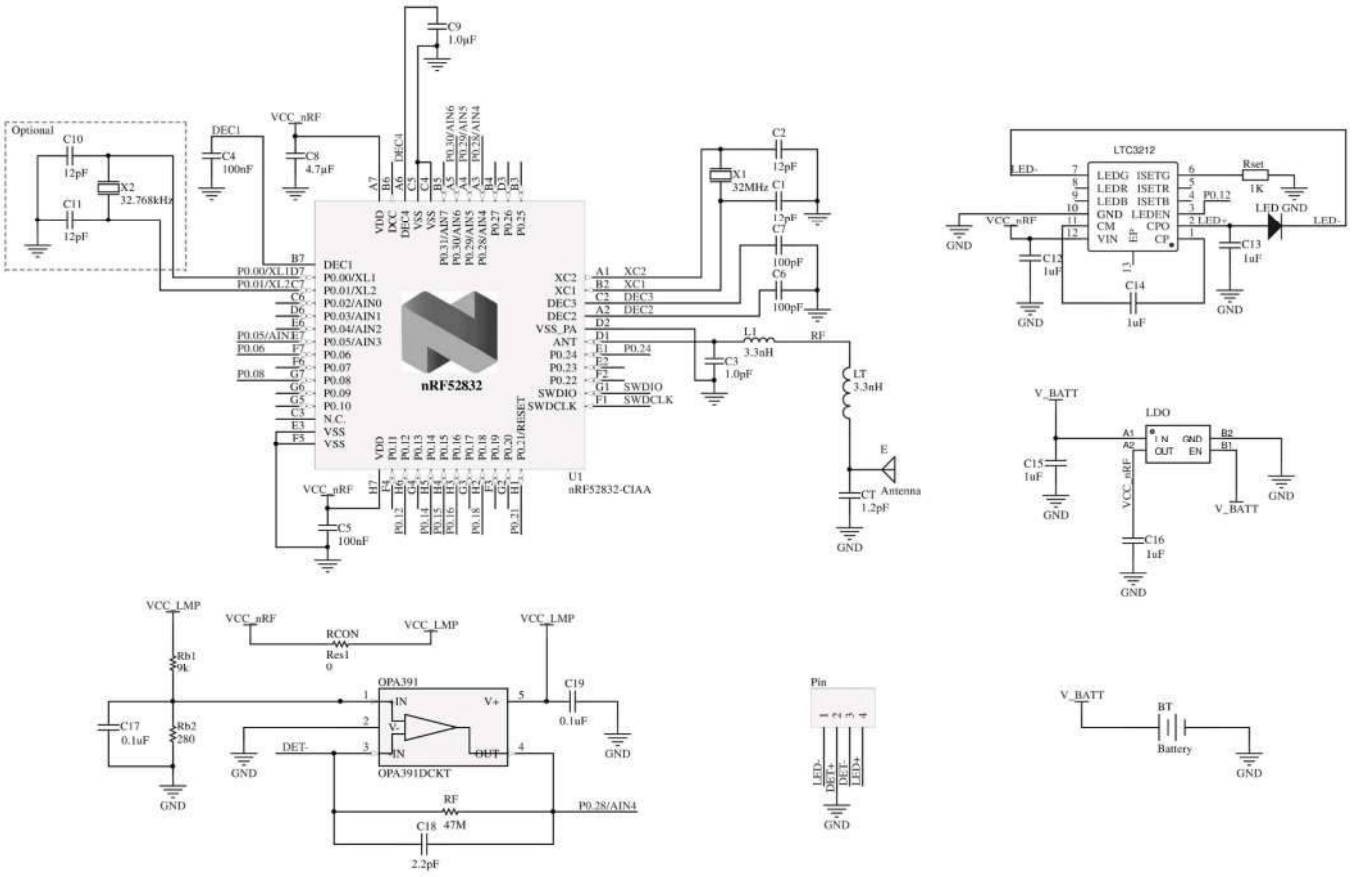

Figure S6. Detailed circuit design diagram of the wireless circuit system.

Figure S7

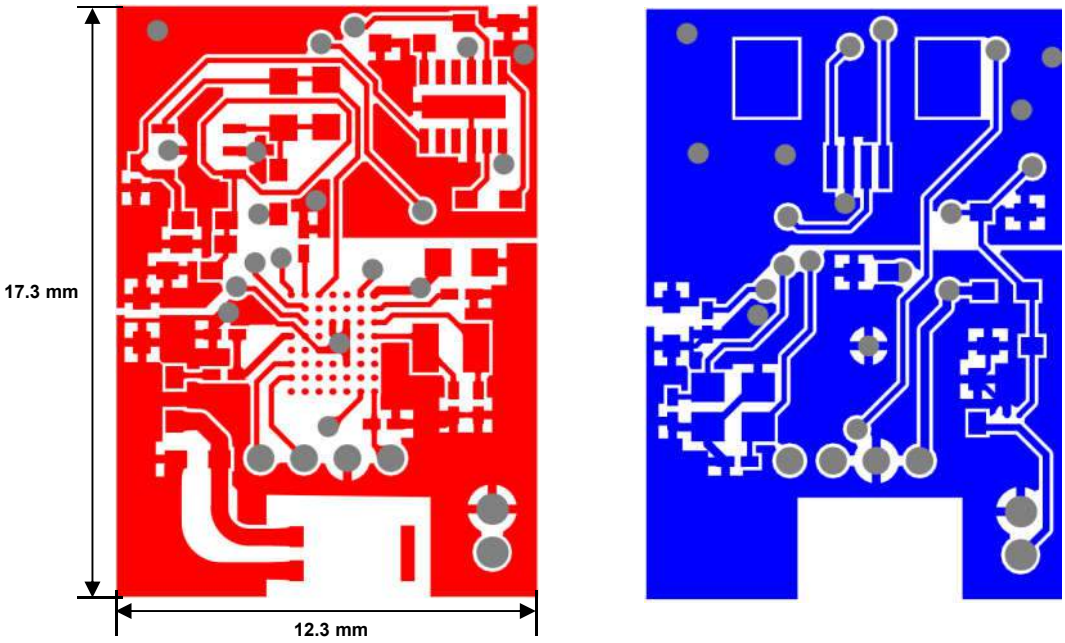

Figure S7. Layout of the designed printed circuit board for the wireless, battery-powered circuit system (red, top layer; blue, bottom layer).

Figure S8

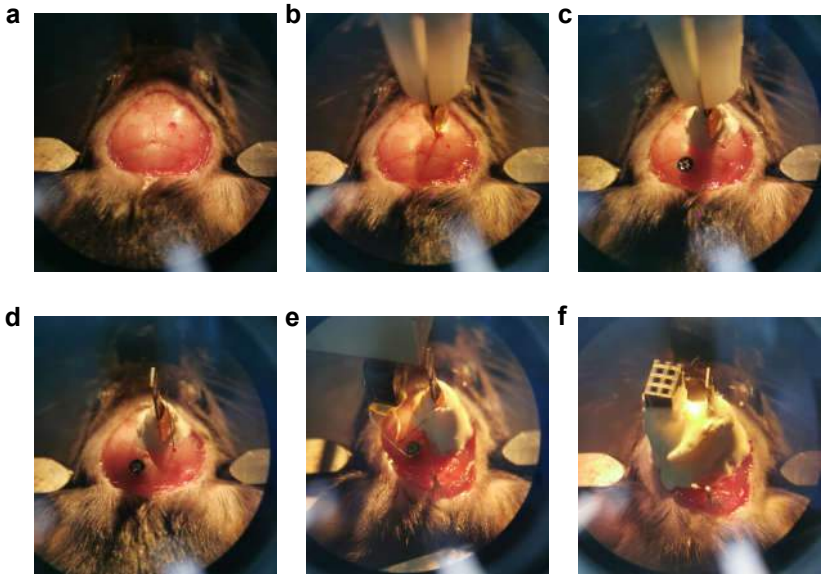

Figure S8. Photographs showing the surgical procedure of implanting a $PbtO_2$ sensing probe as well as recording and stimulation electrodes into the mouse hippocampus. (a) Expose the skull, and drill a hole on the skull. (b) Implant the probe into mouse brain. (c) Apply dental cements to fix the probe to the skull, and implant a screw as a reference electrode. (d) Implant stimulation and recording electrodes into the brain. (e) Fix the electrodes with dental cements. (f) Wire the electrodes to a connector, and apply more dental cements to fix all components.

Figure S9

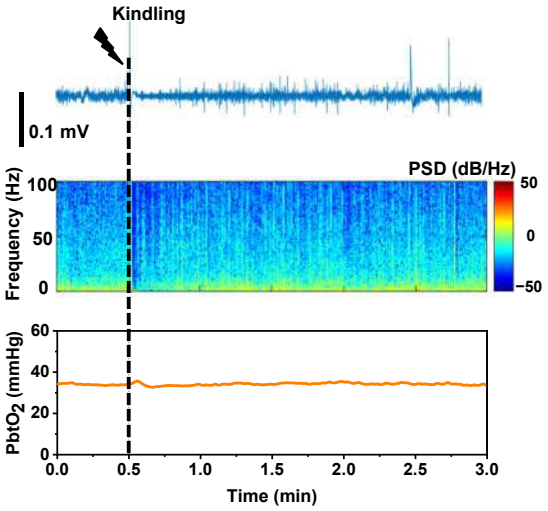

Figure S9. Simultaneously recorded electrophysiological activities in CA1 and $PbtO_2$ in CA3 under kindling from a mouse without afterdischarge. Top: LFP trace. Middle: power spectral density (PSD) of LFP. Bottom: $PbtO_2$.

Figure S10

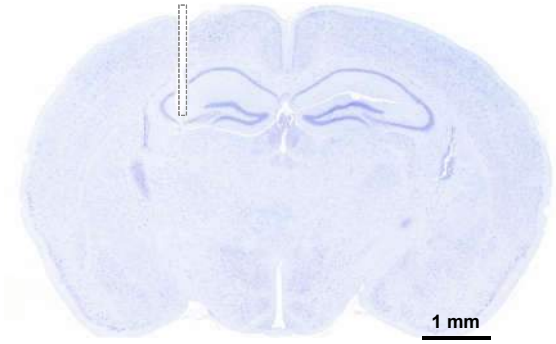

Figure S10. Coronal section stained with Nissl, showing the lesion region in the hippocampus (CA3) of mice created by the probe.

Figure S11

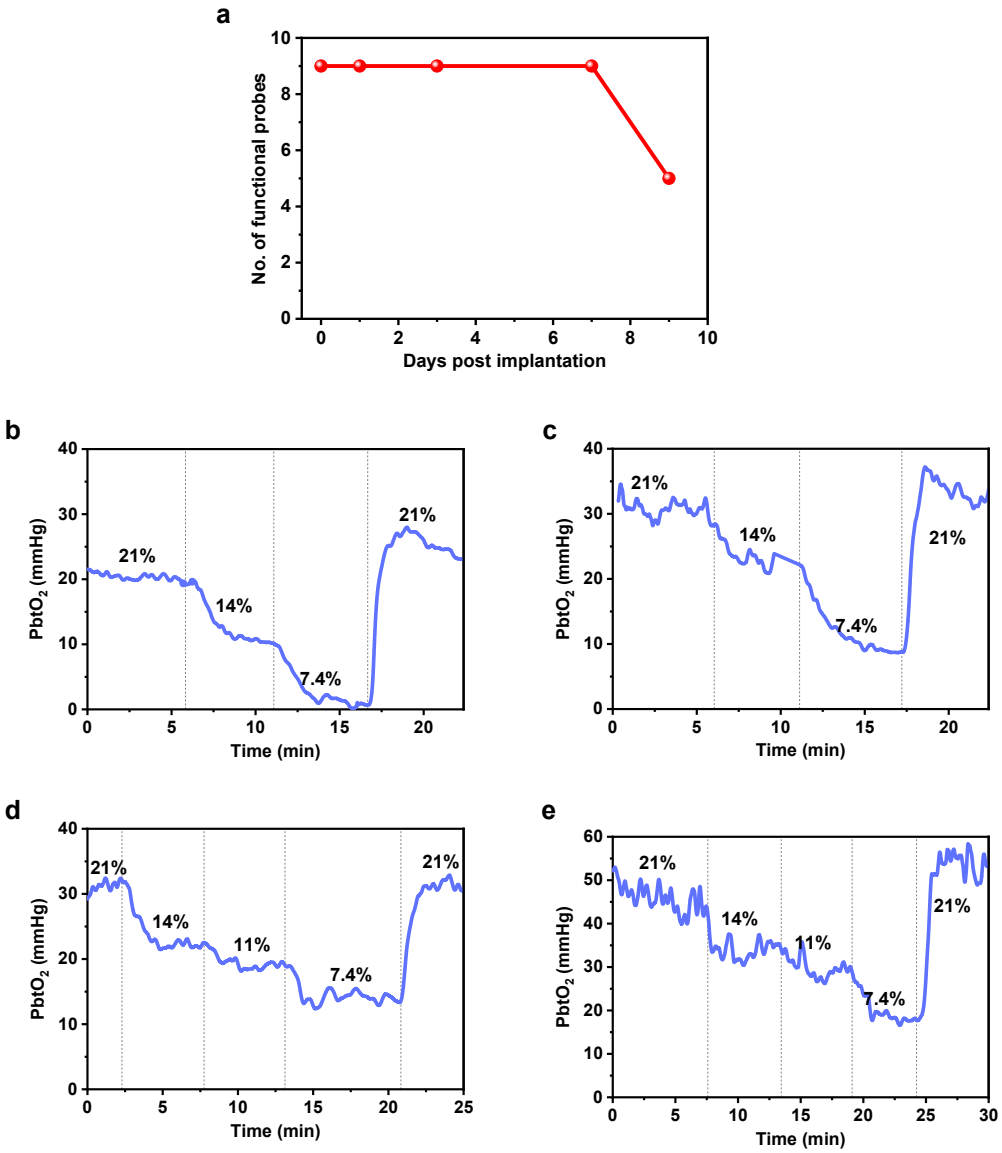

Figure S11. (a) Chronic stability of the implant probes. 9 probes are separately implanted into 9 behaving mice. Recorded $PbtO_2$ from a representative probe with changed FiO_2 after implantation for (b)1, (c) 3, (d) 7, and (e) 9 days.

Figure S12

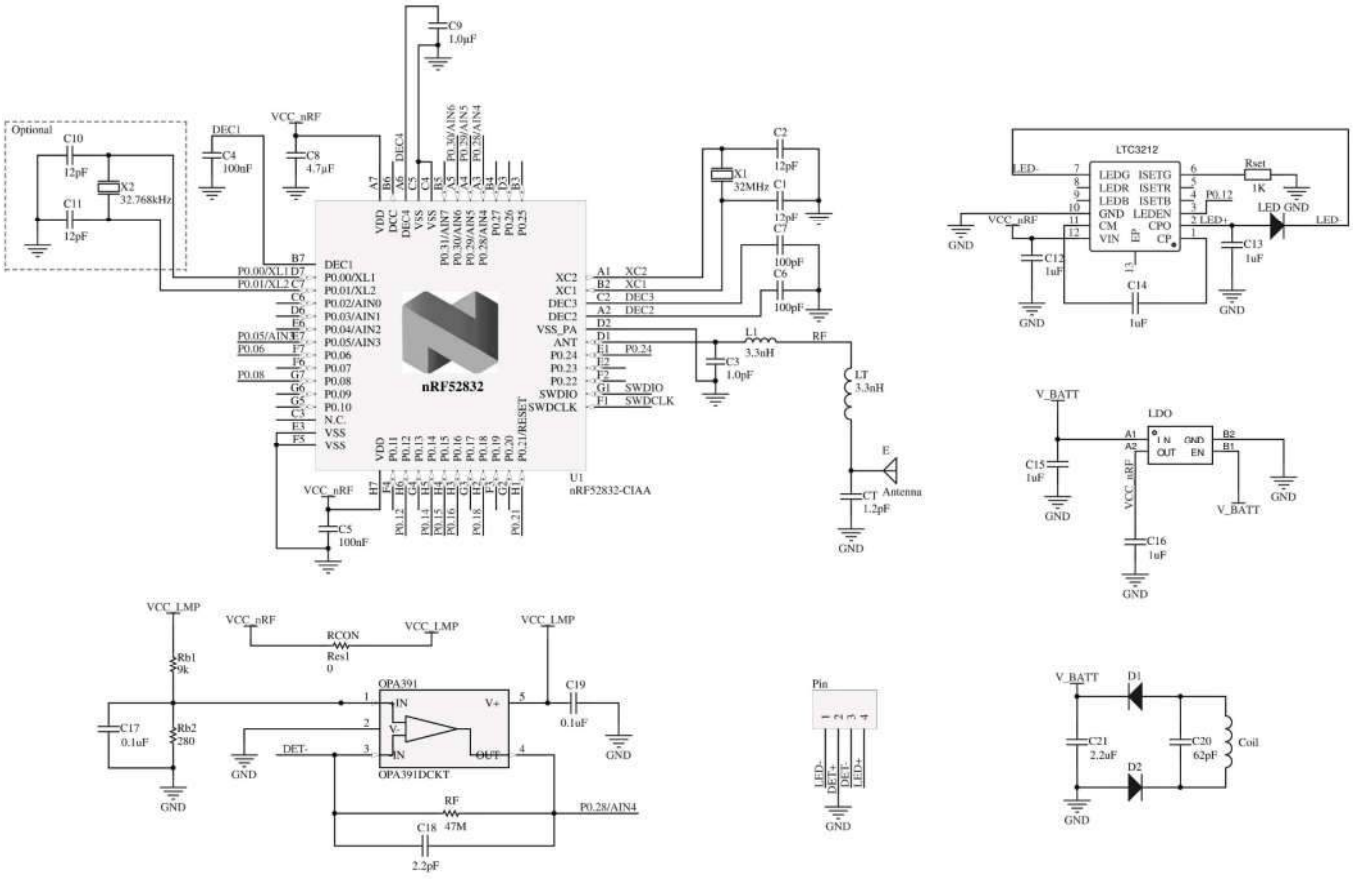

Figure S12. Detailed circuit design diagram of the wireless, battery-free circuit system.

Figure S13

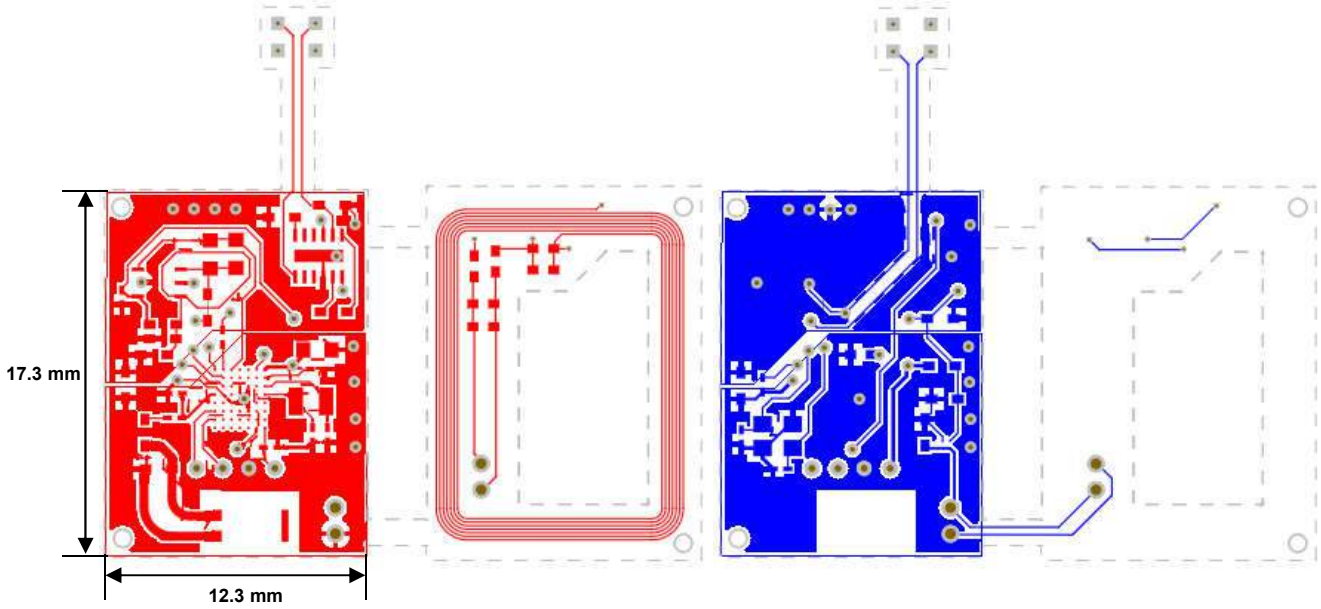

Figure S13. Layout of the designed printed battery-free circuit board for the wireless, battery-free circuit system (red, top layer; blue, bottom layer).

Figure S14

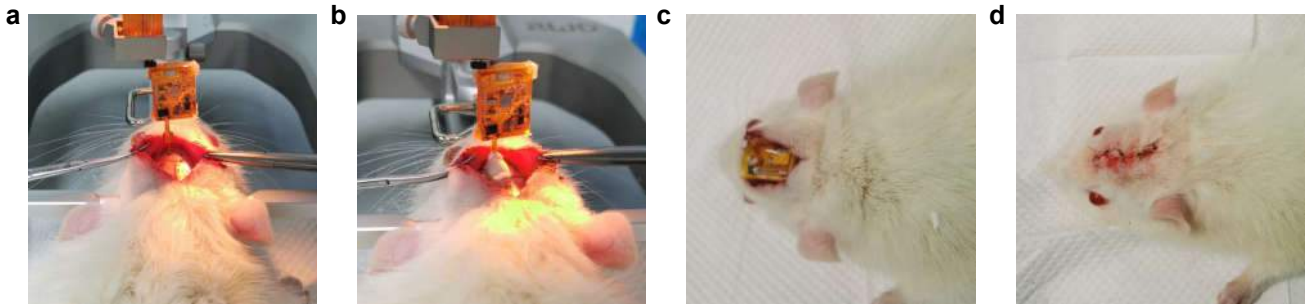

Figure S14. Photographs showing the surgical procedure of implanting a probe and its associated battery-free circuit in a rat. (a) Expose the skull, drill a hole on the skull and implant the probe into the rat brain. (b) Apply the dental cement to fix the probe to the skull. (c) Place the circuit underneath the skin. (d) Suture the skin.

Figure S15

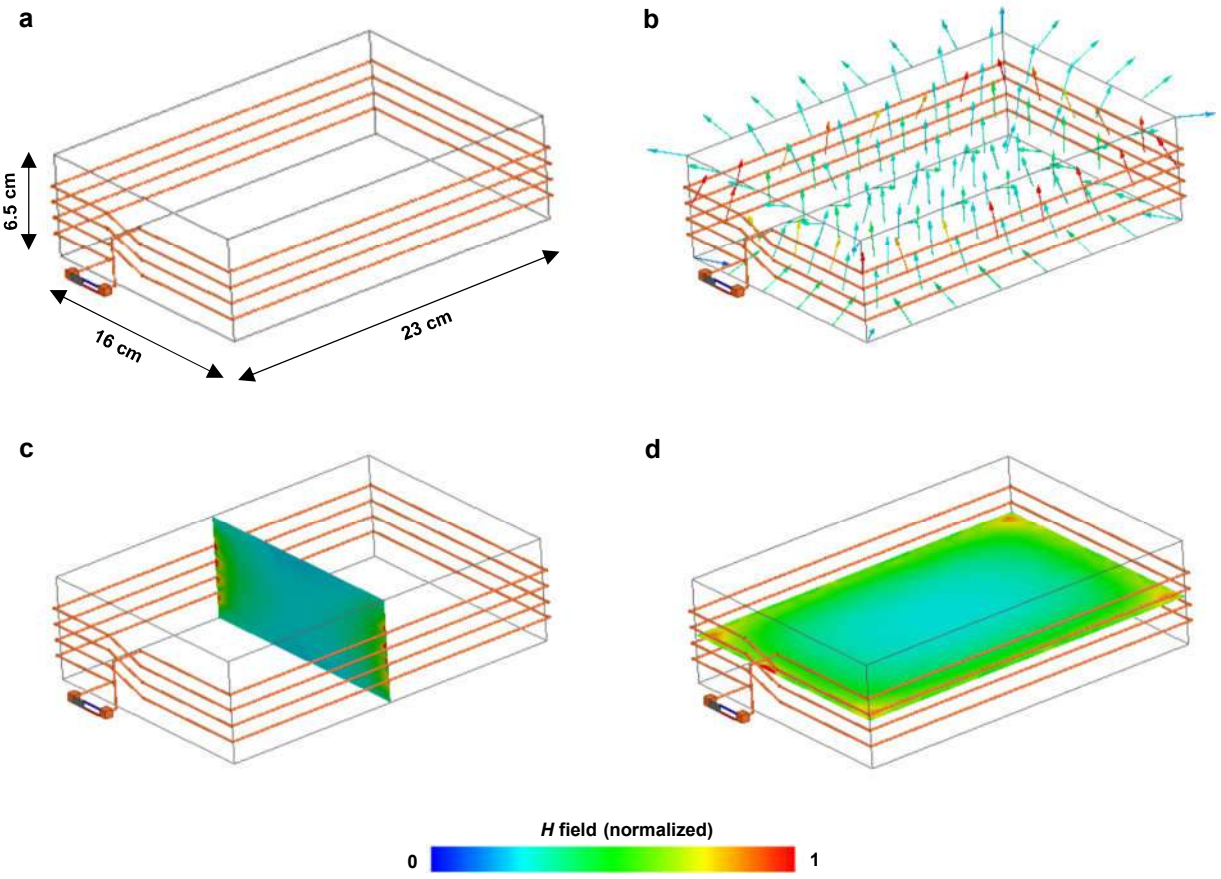

Figure S15. (a) Schematic illustration of the antenna system for wireless power transfer (dimension: $W \times L \times H = 16$ cm $\times$ 23 cm $\times$ 6.5 cm). (b) Simulated magnetic field distribution (normalized) inside the box. (c) Longitudinal and (d) Cross-sectional view of the field distribution.

Figure S16

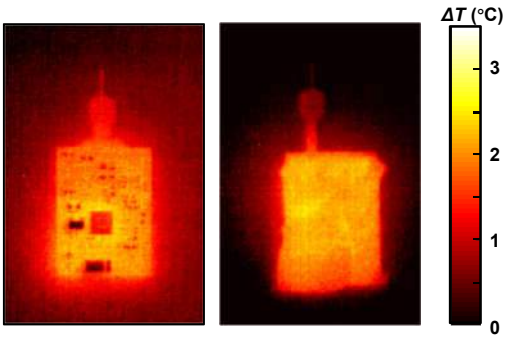

Figure S16. Thermal properties of wireless circuits. (a) Battery-powered circuit. (b) Inductively powered, battery-free circuit (coated with PDMS).

Table S1

Materials	Thickness (nm)
ITO	150
p+ GaN	150
Electron blocking layer	50
MQWs	140
n+ GaN	3000
U GaN	5800
sapphire substrate	-

Table S1. Epitaxial structure of the InGaN violet LED wafer.

Table S2

Materials	Thickness (nm)	Doping (cm^{-3})	Dopant
n+ $In_{0.5}Al_{0.7}Ga_{0.3}P$ filter	500	2e18	Si
n+ GaAs contact	10	>6e18	Si
n+ $In_{0.5}Al_{0.25}Ga_{0.25}P$ window	30	5e18	Si
n+ $In_{0.5}Ga_{0.5}P$ emitter	100	2e18	Si
p $In_{0.5}Ga_{0.5}P$ base	1000	3e16	Zn
p+ $In_{0.5}Al_{0.25}Ga_{0.25}P$ BSF	100	2e18	Mg
p+ GaAs contact	100	>5e18	Mg
p+ $In_{0.5}Ga_{0.5}P$ support	1000	2e18	Mg
$Al_{0.95}Ga_{0.05}As$ sacrificial	500	undoped	-
GaAs substrate	-	-	-

Table S2. Epitaxial structure of the InGaP based detector wafer.

Table S3

Symbol	Component	Package
RJ, RCON, RG2, RG1	Resistor, 0 Ω	R0402
RF	Resistor, 100 MΩ	R0603
R1	Resistor, 280 Ω	R0402
R2	Resistor, 9 kΩ	R0402
C19	Capacitor, 0.1 μF, NP0	C0201
C12, C13, C14, C15, C16	Capacitor, 1 μF, NP0	C0402
C18	Capacitor, 2.2 pF, NP0	C0603
C17	Capacitor, 0.1 μF, NP0	C0402
LDO	NCP161AFCS330T2G	WCSP (4)
OPA391	OPA391DCKR	SC70 (5)
BT	XH-2A	P = 1.25 mm
Pin	F0502-B-04-20T-R	SMD, P = 0.5 mm
LTC3212	LTC3212EDDB	12-LEAD (3 × 2) mm
C1, C2, C10, C11	Capacitor, 12 pF, NP0	C0201
C3	Capacitor, 1.0 pF, NP0	C0201
C4, C5	Capacitor, 100 nF, X7R	C0201
C6, C7	Capacitor, 100 pF, NP0	C0201
C8	Capacitor, 4.7 μF, X5R	C0603
C9	Capacitor, 1.0 μF, X5R	C0402
L1	Inductor, 3.3 nH	L0201
U1	nRF52832-CIAA	WLCSP_C50
X1	XTAL SMD 2016, 32 MHz, CI = 8 pF, Total Tol: ±40 ppm	XTAL_2016
X2	XTAL SMD 2012, 32.768 kHz, CI = 9 pF, Total Tol: ±50 ppm	XTAL_2012
CT	Capacitor, 1.2 μF, NP0	C0402
LT	Inductor, 3.3 nH	L0402
E	H2U34WGTQW0100	SMD, 3.2 × 1.6 × 1.2 mm^3
C20	Capacitor, 62 pF, NP0	C0402
C21	Capacitor, 2.2 μF, NP0	C0402
D1, D2	Schottky diode	DFN1006
Battery	Rechargeable lithium ion battery 3.7 V, 45 mAh	-

Table S3. List of components used in the wireless circuit systems powered by a battery or an RF coil.

Table S4

Ref.	Monitoring target	Operational principle	Monitored body part	Cross-sectional area of the probe	Temporal response	Resolution/ Sensitivity	Device weight
1	oxygen saturation	Optical absorption of HbO_2 and Hb	Brains of rodents	400 × 200 μm^2	~ 0.6 ms (pulse frequency)	7%	0.083 g
2	oxygen saturation	Optical absorption of HbO_2 and Hb	Brains of rodents	600 × 160 μm^2	< 0.1 s (pulse frequency)	2.9%	Wired
3	oxygen pressure	Electro chemical	Muscles of rabbits	500 μm in diameter	20 s	−2.496 nA/mm Hg	Wired
4	oxygen pressure	Electro chemical	Brains of rodents	180 μm in diameter	< 1 s	183 ± 14 pA/μM	9.6 g
5	oxygen pressure	Electro chemical	Lungs of sheep	2.8 × 1.4 mm^2	< 1 s	−0.595 ± 0.009 nA/kPa	Wired
6	oxygen pressure	Electro chemical	Brains of rodents	7 μm in diameter	5.99 ~ 8.04 s	0.85 ± 0.04 nA/μM	Wired
7	oxygen pressure	PL quenching	Kidneys of rodents	3 mm in diameter	< 5 min	–	Wired
8	oxygen pressure	PL quenching	Muscles of sheep	3 × 4.5 × 1.2 mm^3	~210 s	~0.3 °/mm Hg at pO_2 = 10 mmHg	~0.0174 g
9	oxygen pressure	PL quenching	–	420 μm in diameter	~6 s	~0.02 mmHg at pO_2 = 7.6 mmHg	Wired
This work	oxygen pressure	PL quenching	Brains of rodents	330 × 200 μm^2	0.9 s	< 0.8 mmHg at pO_2 = 3.8 mmHg	1.8 g /0.8 g (w/ and w/o battery)

Table S4. Comparing characteristic parameters of wireless and wired implantable oxygenation sensors reported in the literature and this work.

References:

1. Zhang H, et al. Wireless, battery-free optoelectronic systems as subdermal implants for local tissue oximetry. Science advances 2019, 5(3): eaaw0873.
2. Bai W, et al. Bioresorbable photonic devices for the spectroscopic characterization of physiological status and neural activity. Nat Biomed Eng 2019, 3, 644–654.
3. Rivas L, et al. Micro-needle implantable electrochemical oxygen sensor: ex-vivo and in-vivo studies. Biosensors and Bioelectronics 2020, 153: 112028.
4. Bazzu G, et al. Real-time monitoring of brain tissue oxygen using a miniaturized biotelemetric device implanted in freely moving rats. Analytical chemistry 2009, 81(6): 2235-2241.
5. Marland JRK, et al. Real-time measurement of tumour hypoxia using an implantable microfabricated oxygen sensor. Sensing and Bio-Sensing Research 2020, 30: 100375.
6. Zhou L, et al. In vivo monitoring of oxygen in rat brain by carbon fiber microelectrode modified with antifouling nanoporous membrane. Analytical chemistry 2019, 91(5), 3645-3651.
7. Hirakawa Y, et al. Quantitating intracellular oxygen tension in vivo by phosphorescence lifetime measurement. Scientific Reports 2015, 5(1): 1-10.
8. Sonmezoglu S, et al. Monitoring deep-tissue oxygenation with a millimeter-scale ultrasonic implant. Nature Biotechnology 2021, 39(7): 855-864.
9. Commercial Ocean Insight optical oxygen sensors. NEOFOX-GT, probe: FOSPOR-AL300